JGR Space Physics

RESEARCH ARTICLE
10.1029/2022JA030705

Special Section:
Fifteen Years of THEMIS Mission

Thinning of the Magnetotail Current Sheet Inferred From Low-Altitude Observations of Energetic Electrons

A. V. Artemyev[1,2], V. Angelopoulos[1], X.-J. Zhang[1,3], A. Runov[1], A. Petrukovich[2], R. Nakamura[4], E. Tsai[1], and C. Wilkins[1]

[1]Department of Earth, Planetary, and Space Sciences, University of California, Los Angeles, CA, USA, [2]Space Research Institute, Russian Academy of Sciences, Moscow, Russia, [3]Department of Physics, University of Texas at Dallas, Richardson, TX, USA, [4]Space Research Institute, Austrian Academy of Science, Graz, Austria

Key Points:

- The dynamics of plasma sheet (PS) energetic electron fluxes at low altitudes is examined during substorm growth phase
- The PS magnetic projection to low altitudes shrinks in latitude because of magnetic field reconfiguration during growth phase
- Equatorial current sheet thinning is well monitored by energetic electron fluxes at low altitudes

Supporting Information:

Supporting Information may be found in the online version of this article.

Correspondence to:

A. V. Artemyev,
aartemyev@igpp.ucla.edu

Citation:

Artemyev, A. V., Angelopoulos, V., Zhang, X.-J., Runov, A., Petrukovich, A., Nakamura, R., et al. (2022). Thinning of the magnetotail current sheet inferred from low-altitude observations of energetic electrons. *Journal of Geophysical Research: Space Physics*, *127*, e2022JA030705. https://doi.org/10.1029/2022JA030705

Received 31 MAY 2022
Accepted 15 SEP 2022

Abstract The magnetospheric substorm is a key mode of flux and energy transport throughout the magnetosphere associated with distinct and repeatable magnetotail dynamical processes and plasma injections. The substorm growth phase is characterized by current sheet thinning and magnetic field reconfiguration around the equatorial plane. The global characteristics of current sheet thinning are important for understanding of magnetotail state right before the onset of magnetic reconnection and of the key substorm expansion phase. In this paper, we investigate this thinning at different radial distances using plasma sheet (PS) energetic (>50 keV) electrons that reach from the equator to low altitudes during their fast (∼1 s) travel along magnetic field lines. We perform a multi-case study and a statistical analysis of 34 events with near-equatorial observations of the current sheet thinning by equatorial missions and concurrent, latitudinal crossings of the ionospheric projection of the magnetotail by the low-altitude Electron Losses and Fields Investigation (ELFIN) CubeSats at approximately the same local time sector. Energetic electron fluxes thus collected by ELFIN provide near-instantaneous (<5 min duration) radial snapshots of magnetotail fluxes. Main findings of this study confirm the previously proposed concepts with low-altitude energetic electron measurements: (a) Energy distributions of low-altitude fluxes are quantitatively close to the near-equatorial distributions, which justifies the investigation of the magnetotail current sheet reconfiguration using low-altitude measurements. (b) The magnetic field reconfiguration during the current sheet thinning (which lasts ≥ an hour) results in a rapid shrinking of the low-altitude projection of the entire PS (from near-Earth, ∼10R_E, to the lunar orbit ∼60R_E) to 1–2° of magnetic latitude in the ionosphere. (c) The current sheet dipolarization, common during the substorm onset, is associated with a very quick (∼10 min) change of the tail magnetic field configuration to its dipolar state, as implied by a poleward expansion of the PSPS at low altitudes.

1. Introduction

Substorms, one of the most energetic phenomena in the Earth's magnetosphere, starts with the growth phase, characterized by the formation of a thin elongated magnetotail current sheet (e.g., Angelopoulos, McFadden, et al., 2008; Baker et al., 1996; Sitnov et al., 2019, and references therein), that is, the so-called current sheet thinning (see review by Runov et al., 2021, and references therein). Such current sheet thinning ends with a current sheet instability on ion (see, e.g., Coppi et al., 1966; Schindler, 1974; Galeev & Zelenyĭ, 1977; Sitnov et al., 2013) or electron (see, e.g., Pellat et al., 1991; Pritchett, 2005; Pritchett et al., 1991; Liu et al., 2014; Lu et al., 2020) scales, resulting in the magnetic field line reconnection (and subsequent reconfiguration, i. e., the so-called dipolarization) that mark the substorm onset (see discussion of various onset scenarios in Sitnov et al., 2013, 2017). The reconnection process and the efficiency of magnetic field energy conversion to particle kinetic energy are highly dependent upon the pre-reconnection thin current sheet configuration (see discussion in An et al., 2022; Lu, Artemyev, Angelopoulos, Pritchett, & Runov, 2019; Pritchett & Coroniti, 2011; Pritchett et al., 1997; Sitnov, Motoba, & Swisdak, 2021; Sitnov et al., 2002; Zelenyi et al., 2008). Therefore, investigation of the growth-phase current sheet thinning and configuration is important for understanding the dynamics the magnetotail prior to and during substorm onset.

The main signatures of the current sheet thinning are a decrease of the equatorial magnetic field B_z (hereinafter Geocentric Solar Magnetospheric (GSM) coordinates are used), an increase of the equatorial current density j_y, and a less-pronounced increase of the lobe magnetic field B_L (see, e.g., Birn et al., 1998; Schindler & Birn, 1982, 1993). These signatures are quite repeatable and well-documented by a number of authors using

past single and more recent multi-spacecraft missions (Artemyev, Angelopoulos, Runov, & Petrukovich, 2016; Petrukovich et al., 2007; Sergeev et al., 2011; Snekvik et al., 2012; Yushkov et al., 2021). Simulations using magnetohydrodynamical (MHD) analytical models (e.g., Birn et al., 2004), numerical 3D MHD (e.g., Gordeev et al., 2017; Hsieh & Otto, 2015), hybrid (Lu, Artemyev, Angelopoulos, Lin, et al., 2019; Lu et al., 2016) and particle-in-cell (e.g., Lu et al., 2018) approaches also reproduce these signatures rather faithfully. Thus, the thinning process during the substorm growth phase has been well established based on recent near-equatorial spacecraft observations and numerical simulations (see reviews by Runov et al., 2021; Sitnov et al., 2019). However, spatial scales of the current sheet reconfiguration are less understood. Equatorial spacecraft observations have unveiled the local thinning and the following depolarization (magnetotail reconfiguration) processes, but cannot address typical scales of the thin current sheet along the magnetotail (along GSM x). This thin current sheet can be formed locally within the near-Earth magnetotail (see simulation results in Gordeev et al., 2017; Hsieh & Otto, 2015) or can continue from the near-Earth tail to the lunar orbit (see discussion in Angelopoulos et al., 2013; Artemyev et al., 2019). One useful approach for simultaneous probing of the magnetotail current sheet configuration over a large x-range is the remote sensing of the magnetotail via low-altitude measurements of energetic particle fluxes.

In the near-Earth magnetotail, energy and pitch-angle distributions of equatorial particles strongly vary with the radial distance. Low-altitude measurements, therefore, can provide a good estimate on the radial distance where magnetic field changes its configuration (see examples in Dubyagin et al., 2002; Newell et al., 1998; Sergeev, Malkov, & Mursula, 1993; Sergeev et al., 1983). The most developed technique is to examine the anisotropy of supra-thermal plasma sheet (PS) ions (~10–30 keV), because the latitude of isotropy for a given energy (i.e., the latitude where the ratio of precipitating to trapped fluxes at low altitudes approaches unity) reveals the equatorial magnetic field curvature and thus the magnetic field configuration that can pitch-angle scatter these ions toward isotropy (e.g., Dubyagin et al., 2021; Sergeev et al., 2018). On the other hand, electrons at similar energies can be predominantly pitch-angle scattered and precipitate to the ionosphere by various wave-particle interactions (see reviews Khazanov et al., 2017; Ni et al., 2016; Nishimura et al., 2020); more energetic electrons (>50 keV), however, are also suitable to infer the isotropy boundary, similar to 10–30 keV ions (e.g., Sergeev et al., 2012, 2018; Yahnin et al., 1997), because they are expected to be isotropized by curvature scattering in the PS and their low-altitude fluxes should be comparable to the equatorial fluxes in the PS. The isotropy boundary location is closely related to the location of the near-Earth edge of the thin current sheet, but this boundary is energy dependent. The integral fluxes for a couple of energy ranges (typically available at Polar Operational Environmental Sattelite (POES) spacecraft and widely used for probing the magnetotail at low altitudes; see, e.g., Dubyagin et al. (2018); Sergeev et al. (2015)) localize the inotropy boundary, but are insufficient to unravel the entire magnetotail reconfiguration from near Earth to the lunar orbit. Therefore, in this study we utilize the new data set of differential electron fluxes from low-altitude Electron Losses and Fields Investigation (ELFIN) CubeSats (Angelopoulos et al., 2020). We aim to

- demonstrate that ELFIN measurements can be used to probe the magnetotail magnetic field configuration with many more details than it was available with POES data set. For this reason we combine measurements from near-equatorial Time History of Events and Macroscale Interactions during Substorms (THEMIS) spacecraft (Angelopoulos, 2008) and from ELFIN to compare their energetic electron flux magnitudes and energy spectra (flux v. s. energy profiles) during the current sheet thinning. Similarity of the equatorial and low-altitude energy spectra in the near-Earth magnetotail indicates a conjunction between THEMIS and ELFIN in this region.
- demonstrate that the magnetic reconfiguration during the current sheet thinning may occur over a large radial distances, down to the lunar orbit. For this reason we combine measurements from ELFIN, near-Earth THEMIS, middle tail ($\sim 20 - 30 R_E$) Magnetospheric Multiscale Mission (MMS) (Burch et al., 2016), and lunar distant Acceleration, Reconnection, Turbulence and Electrodynamics of the Moon's Interaction with the Sun (ARTEMIS) (Angelopoulos, 2011).
- demonstrate that magnetic field reconfiguration during the current sheet thinning shrinks the PS projection (for [50, 300] keV electrons) to a couple of degrees (in latitudes) at low altitudes.

Most results from this study have been proposed and demonstrated via analysis of POES measurements and various numerical and empirical modeling of the magnetotail. Therefore, our study is mainly confirm these results

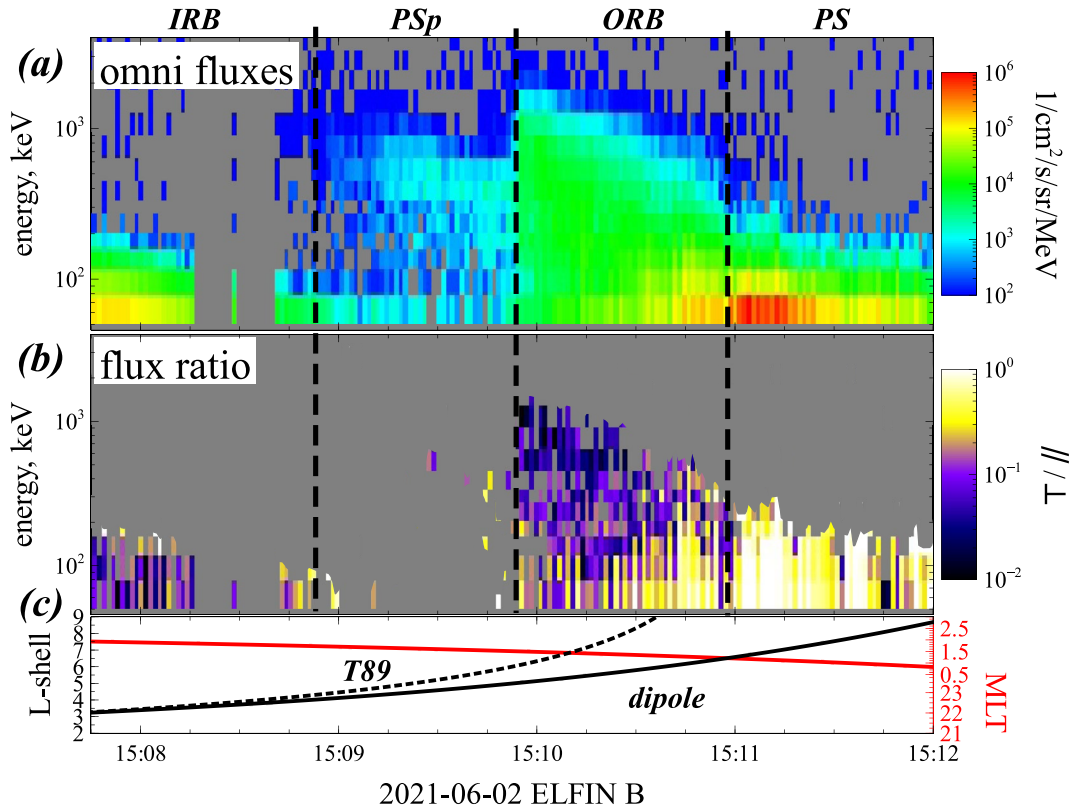

Figure 1. Overview of Electron Losses and Fields Investigation (ELFIN)-B observations during one example trajectory on 2 June 2021. (a) Omni-directional electron fluxes, (b) the ratio of precipitating (within the bounce loss cone) and trapped (outside of the bounce loss cone) fluxes, and (c) ELFIN *L*-shell and magnetic local time. Labels on the top mark different regions of the magnetosphere: inner radiation belt (IRB), plasmasphere (PSp), outer radiation belt (ORB), plasma sheet (PS).

about magnetotail reconfiguration with the new data set from ELFIN, which for the first time enables a direct comparison of low-altitude and equatorial energy spectra of electrons.

The paper consists of five sections. In Section 2 we describe the available datasets, spacecraft instruments and measurements. Overview figures for all the collected events can be found in Supporting Information S1. In Section 3 we analyze a few events in detail. Section 3.1 describes the typical evolution of equatorial distributions of energetic electrons versus radial distance as inferred from low-altitude during current sheet thinning. Comparison of ELFIN and THEMIS measurements shows repeatable patterns of association between low-altitude and equatorial energetic electron fluxes, and reveals the temporal evolution of the current sheet configuration. Section 3.2 extends the comparison of low-altitude and equatorial fluxes to distances $>13R_E$ by including MMS and ARTEMIS observations. Section 3.3 focuses on the time-scale of the magnetic field reconfiguration as traced by energetic electrons around substorm onset. In Section 4 we describe the results of a statistical analysis of the THEMIS—ELFIN conjunction database of current sheet thinning and dipolarization intervals. In Section 5 we summarize our results.

2. Instruments and Data Sets

We use both ELFIN (Angelopoulos et al., 2020) CubeSats (ELFIN A and B) to examine the low-altitude energetic (>50 keV) electrons from the PS. ELFIN moves in a polar, near circular orbit at ~450 km altitude, with an orbital period of ~1.5 hr. Its energetic particle detector measures electron fluxes from ~50 keV to ~7 MeV with a 22.5° pitch-angle resolution and 1.5 s (half-spin) time resolution. A typical example of electron fluxes during an ELFIN trajectory is shown in Figure 1. The projection of ELFIN to the equatorial plane (Panel (c)) exhibits only a small magnetic local time (MLT) variation, as expected from ELFIN's high-latitude polar orbit. The Earth-interior only field (based on the International Geophysical Reference System (IGRF)) has been used to estimate the equatorial

projection of ELFIN in R_E (its L-shell) and it is shown in solid line in the same panel. In addition, the same projection was computed from the T89 (Tsyganenko, 1989) magnetic field model, that includes external currents (such as the magnetopause and ring currents), and is shown in dashed line. The former (IGRF projection) is good in the inner magnetosphere (L < 6–9), but its mapping uncertainty becomes too large, beyond that distance and we rely on the latter (T89 projections) in the PS (L > 9). We use these models only to provisionally separate inner magnetosphere and PS observations. We then independently refine those regions and their separation using electron energy spectra. The omni-directional electron fluxes in Panel (a) and the ratio of precipitating to trapped electron fluxes Panel (b) clearly display signatures typical of different regions in the magnetosphere:

- At L > 6, when fluxes above 10^3#/cm^2/s/sr/MeV are of low energy (<200 keV), isotropic, and have no significant variation with L, they denote PS (after 15:11:25 UT).
- A strong increase of energies (from <200 to >200 keV) corresponding to flux level >10^3#/cm^2/s/sr/MeV at decreasing L values defines the interface region between PSPS and the inner magnetosphere (around 15:11:00-15:11:15UT). This interface region has a finite width and may include the so-called isotropy boundary where equatorial fluxes at low pitch angles, reaching ELFIN, increase with decreasing L, see Imhof et al. (1977); Sergeev and Tsyganenko (1982).
- The outer radiation belt (15:09:45-15:11:00 UT) is observed at lower L from the interface region and is characterized by L-dependent fluxes of relativistic electrons (flux level is above 10^3#/cm^2/s/sr/MeV for >500 keV) with strong flux anisotropy: precipitating fluxes are generally much lower than trapped fluxes, except transient precipitation bursts driven by wave-particle interactions (see details in Mourenas et al., 2021).
- The plasmasphere (15:08:45-15:09:45) is observed at lower L from the outer radiation belt and is characterized by strong decrease of <500 keV fluxes of trapped electrons (in comparison with the outer radiation belt) and near absence of precipitation fluxes (strong flux anisotropy). This is due to the strong pitch-angle anisotropy of sub-relativistic (<500 keV) electrons and the quite weak scattering of relativistic (>500 keV) electrons by whistler-mode hiss waves (e.g., Ma et al., 2016; Mourenas et al., 2017).
- The inner radiation belt (before 15:08:30) is observed at lower L from the plasmasphere and is characterized by presence of only <300 keV trapped fluxes above 10^3#/cm^2/s/sr/MeV.

In the following, we focus on the PS electron fluxes and compare their time-profiles (which are ionospheric projections of radial profiles of equatorial current sheet fluxes) at different stages of the current sheet thinning. Therefore, we are not concerned with separating the different regions within the inner magnetosphere (inner radiation belt, plasmasphere, outer radiation belt), but only to determine the PS as the region with isotropic fluxes at higher-L from its interface with the inner magnetosphere.

Although ELFIN routinely measures pitch-angle resolved electron distributions, in our analysis we only use omni-directional fluxes, because energetic electrons are well isotropized in the PS anyway. For each event we determine the interface region satisfying the following criteria:

- Isotropic fluxes with the magnitude >10^3#/cm^2/s/sr/MeV for energies >200 keV
- Increase of energies corresponding to >10^3#/cm^2/s/sr/MeV fluxes with L-shell decrease
- Located between the plasmasheet (isotropic >10^3#/cm^2/s/sr/MeV fluxes for <200 keV) and the outer radiation belt (anisotropic fluxes with >10^3#/cm^2/s/sr/MeV for >200 keV)

The accuracy of interface determination does not affect conclusions derived for individual events, because for each event we show actual fluxes measured by ELFIN. Figure 2 shows a comparison of such omni-directional ELFIN fluxes, which have been averaged over the region of L > 10 (with an upper limit between 12 and 18 depending on the crossing) during several ELFIN orbits and near-equatorial THEMIS fluxes from the Solid State Telescope (SST, see Angelopoulos, Sibeck, et al., 2008) measurements. THEMIS SST measures pitch-angle resolved electron fluxes between 30 and 700 keV energy at a 3 s time resolution; similar to the ELFIN measurements, we use omni-directional SST fluxes. In Figure 2, THEMIS fluxes are averaged over 1 hr intervals, centered at the L-shell and MLT denoted along the track. There is a relatively stable flux level in the near-Earth PS, at L > 10 (THEMIS A, D, and E apogees are at ~13R_E). Most of the THEMIS electron flux variations at L > 10 (in the PS) are due to magnetotail transients (e.g., PS injections, see Gabrielse et al., 2014, 2017; Nakamura et al., 2009, 2013). Orbit-averaged (for L > 10) ELFIN fluxes are plotted in this figure versus time, and the average MLT during each orbit is depicted as annotation. There are about ~5–10 PS crossings measured at the nightside for each ELFIN satellite per day. In the PS, ELFIN fluxes are quite similar to THEMIS fluxes, because electrons are isotropized in

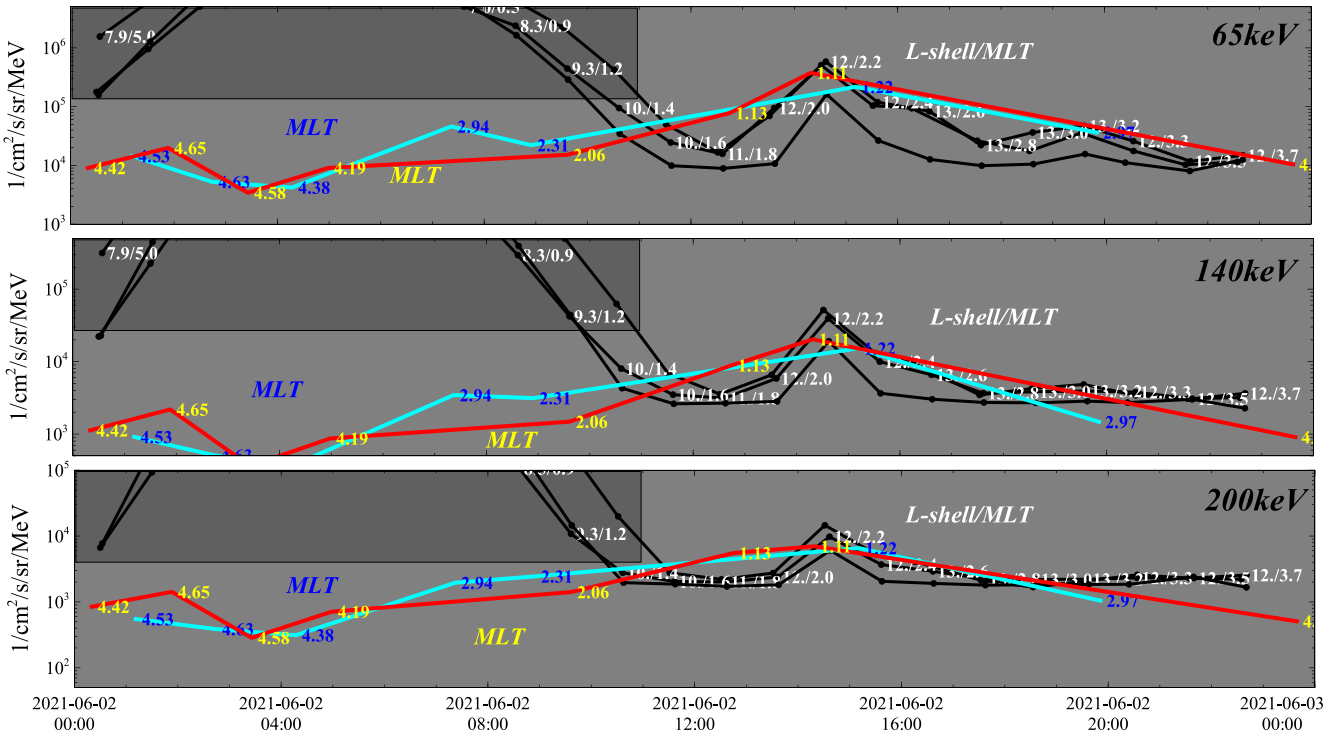

Figure 2. Omni-directional electron fluxes from Time History of Events and Macroscale Interactions during Substorms (THEMIS) SST and Electron Losses and Fields Investigation (ELFIN) energetic particle detector for three different energies. THEMIS fluxes, averaged over ~1 hr time increments, are shown in black, with *L*-shell/magnetic local time (MLT) denoted (three curves for THEMIS A, D, and E, respectively). The shaded regions mark THEMIS fluxes for $L < 9$ where no comparison with ELFIN plasma sheet fluxes is possible. ELFIN fluxes, averaged over each orbit at $L > 10$, are shown in red (ELFIN A) and blue (ELFIN B), with the average MLT denoted.

this region. ELFIN can even trace transient variations of electron fluxes observed by THEMIS (e.g., the local flux increase around 15:00UT). In contrast to the inner magnetosphere, where ELFIN fluxes vary strongly with MLT (see details and discussion in Mourenas et al., 2021), there is no comparably strong dependence of ELFIN fluxes on MLT in the PS, that is, the energetic electron flux gradient along the dawn-dusk direction (e.g., Sarafopoulos et al., 2001) is small enough in the near-Earth PS that we can ignore the MLT dependence in orbit-averaged fluxes at ELFIN. Thus, we will compare measurements from ELFIN and THEMIS without requiring a very strict MLT conjunction between them: we only require that the equatorial projections of ELFIN be within 2 hr of MLT from THEMIS.

Between June–September 2021, ELFIN and THEMIS were at the night-side PS, and the main criteria for our event selection for this study (using data from this period) are:

- THEMIS should observe signatures of the current sheet thinning: B_z decreases, $|B_x|$ increases at the off-equatorial spacecraft (indication of the equatorial current density increase, see Artemyev, Angelopoulos, Runov, and Petrukovich (2016)). This should be followed by a dipolarization, as evidenced by $|B_x|$ going down (PS expansion) and B_z going up (a signature of one or more dipolarization fronts, see Runov et al. (2009)).
- At least one ELFIN spacecraft should traverse the PS within 2 hr before the thinning signatures at THEMIS start, two such traversals by ELFIN should occur during the thinning, and one traversal should take place within 2 hr after the dipolarization onset. Each event should include at least five ELFIN orbits in total.

We collect 30 such intervals (events). Another four events exist with only three ELFIN orbits (instead of five), but are complemented by MMS and/or ARTEMIS observations. MMS and/or ARTEMIS observations are also available during 6 of the 30 events with five ELFIN orbits. ARTEMIS spacecraft have the same set of measurements as THEMIS, but are located at $\sim -60R_E$ downtail (see examples of current sheet thinning observed by THEMIS and ARTEMIS in Artemyev et al., 2019). The MMS spacecraft (Burch et al., 2016) provide magnetic field data (with a resolution of 1/64 s, see Russell et al., 2016) and energetic electron fluxes measured by the

Table 1
List of Events With ELFIN and THEMIS Observations of Energetic Electron Fluxes During the Current Sheet Thinning

#	Date	Time	Equatorial spacecraft
1	02-06-2021	08:00–16:00	THEMIS
2	11-06-2021	01:00–05:30	THEMIS
3	18-06-2021	08:00–15:00	THEMIS
4	20-06-2021	15:40–23:00	THEMIS
5	22-06-2021	02:00–08:00	THEMIS
6	24-06-2021	08:30–15:30	THEMIS
7*	25-06-2021	04:00–10:30	THEMIS, ARTEMIS
8	07&08-07-2021	21:00–03:00	THEMIS
9	30-06-2021	08:30–15:30	THEMIS
10	03-07-2021	01:30–09:30	THEMIS
11	05-07-2021	07:00–15:00	THEMIS
12	07-07-2021	13:30–19:30	THEMIS
13	09&10-07-2021	22:00–03:30	THEMIS
14	10-07-2021	12:00–19:30	THEMIS, MMS
15	12-07-2021	13:30–20:30	THEMIS
16	14-07-2021	18:00–22:00	THEMIS, MMS
17	15-07-2021	00:30–08:00	THEMIS, MMS
18	15-07-2021	16:30–23:30	THEMIS
19	16-07-2021	00:00–08:30	THEMIS
20	19-07-2021	13:30–20:30	THEMIS
21	24-07-2021	05:30–10:30	THEMIS
22	24-07-2021	19:00–23:00	THEMIS, MMS, ARTEMIS
23	27-07-2021	09:40–20:00	THEMIS
24	28-07-2021	01:00–08:00	THEMIS, MMS
25*	28-07-2021	16:00–19:00	THEMIS, MMS
26*	31-07-2021	14:00–21:00	THEMIS, MMS
27	07-08-2021	11:00–15:30	THEMIS
28	06-09-2021	18:30–22:30	THEMIS
29	07-09-2021	18:00–23:30	THEMIS
30	08-09-2021	09:30–18:30	THEMIS
31	15-09-2021	17:00–24:00	THEMIS, MMS
32	16&17-09-2021	19:00–01:00	THEMIS
33*	20-09-2021	00:30–05:00	THEMIS, ARTEMIS
34	22-09-2021	09:00–17:30	THEMIS

Note. Stars (*) show events with only three ELFIN orbits. ARTEMIS, Acceleration, Reconnection, Turbulence and Electrodynamics of the Moon's Interaction with the Sun; ELFIN, Electron Losses and Fields Investigation; MMS, Magnetospheric Multiscale Mission; THEMIS, Time History of Events and Macroscale Interactions during Substorms.

Fly's Eye Energetic Particle Spectrometer (FEEPS; with a resolution of 4s, see Blake et al., 2016) at radial distances $\in [-15, -30]R_E$, which extend near-Earth THEMIS measurements beyond $L = 13$ in the period of interest. Table 1 shows the entire list of events, whereas in Supporting Information S1 contains overview figures for all.

3. Typical Events

In this section we show six typical events from Table 1: the first two, discussed in Section 3.1, serve to demonstrate the general characteristics of the dynamics and evolution of energetic electron fluxes at ELFIN and THEMIS in the near-Earth PS; the next two, in Section 3.2, show similar dynamics using ELFIN, MMS and ARTEMIS at PS distances $L > 13$, and the last two events, in Section 3.3, show PS signatures at times of fast magnetic field reconfiguration, around the time of dipolarization.

3.1. THEMIS and ELFIN Observations: Flux Dynamics During Current Sheet Thinning and Dipolarization

Figure 3 shows THEMIS and ELFIN observations during the current sheet thinning. The THEMIS spacecraft moved tailward from low to high L, (from 08:00 to 11:00 UT, B_z decrease, in Panel (a), because of this THEMIS motion). At around 11:00 UT B_z reached its typical magnitude at the near-Earth PS. After ~11:00 UT, THEMIS measured slow B_z decreases and $|B_x|$ increases (better seen at ThA located farther from the equatorial plane). These are typical signatures of current sheet thinning (see similar observations from THEMIS in Artemyev, Angelopoulos, Runov, & Petrukovich, 2016; Sergeev et al., 2011; Sun et al., 2017). At ~14:30 UT, the current sheet thinning ended with a magnetic field dipolarization (rapid B_z increase, which we interpret as a dipolarization front, accompanied by PS expansion as evidenced by a $|B_x|$ decrease, see Runov et al. (2009), (2011). After 14:30 UT, THEMIS observed a dipolarized magnetotail with large B_z ($>|B_x|$). Current sheet thinning was associated with the current density increase (Petrukovich et al., 2007) and magnetic field reconfiguration, so the THEMIS spacecraft ended up at field lines crossing the equatorial plane farther downtail. This explains the decrease of the energetic electron fluxes from 11:00 to ~14:00 UT (see Panel (b)). The dipolarization brought new energetic fluxes from the reconnection region and also reconfigured the magnetotail magnetic field (which effectively *moved* THEMIS toward the equator) (Gabrielse et al., 2014, 2019). This explains the significant increase of the energetic electron fluxes after 14:00-14:30 UT.

During the interval shown in Figures 3a and 3b, ELFIN A and B collected data on the PS field lines in the ionosphere 5 times while at approximately the same MLT sector as THEMIS. The first two ELFIN orbits at ~09:00 UT and ~09:30 UT show clear signatures of the PS electron fluxes (Panels (c#1, #2)); note that due to gaps in ELFIN measurements we do not determine the PS—outer radiation belt interface for these orbits). At around 08:56 UT (for ELFIN B) and 09:37 UT (for ELFIN A), the ELFIN spacecraft were outside the outer radiation belt (manifested by the absence of strong electron fluxes at >200 keV) at $L > 10$. ELFIN measurements show energetic electrons at <200 keV, with a flux of $\sim 10^4$ #/cm^2/s/sr/MeV at 63 keV. This flux magnitude is slightly below the minimum flux measured by THEMIS D during the current sheet thinning, at ~13:15 UT (large $|B_x|$ implies a THEMIS D projection downtail), see Panel (f#1). Therefore, before the current sheet thinning, ELFIN measured fluxes comparable to the fluxes in the near-Earth tail. The third and fourth available ELFIN data collections at ~12:45 UT and ~14:20 UT occurred

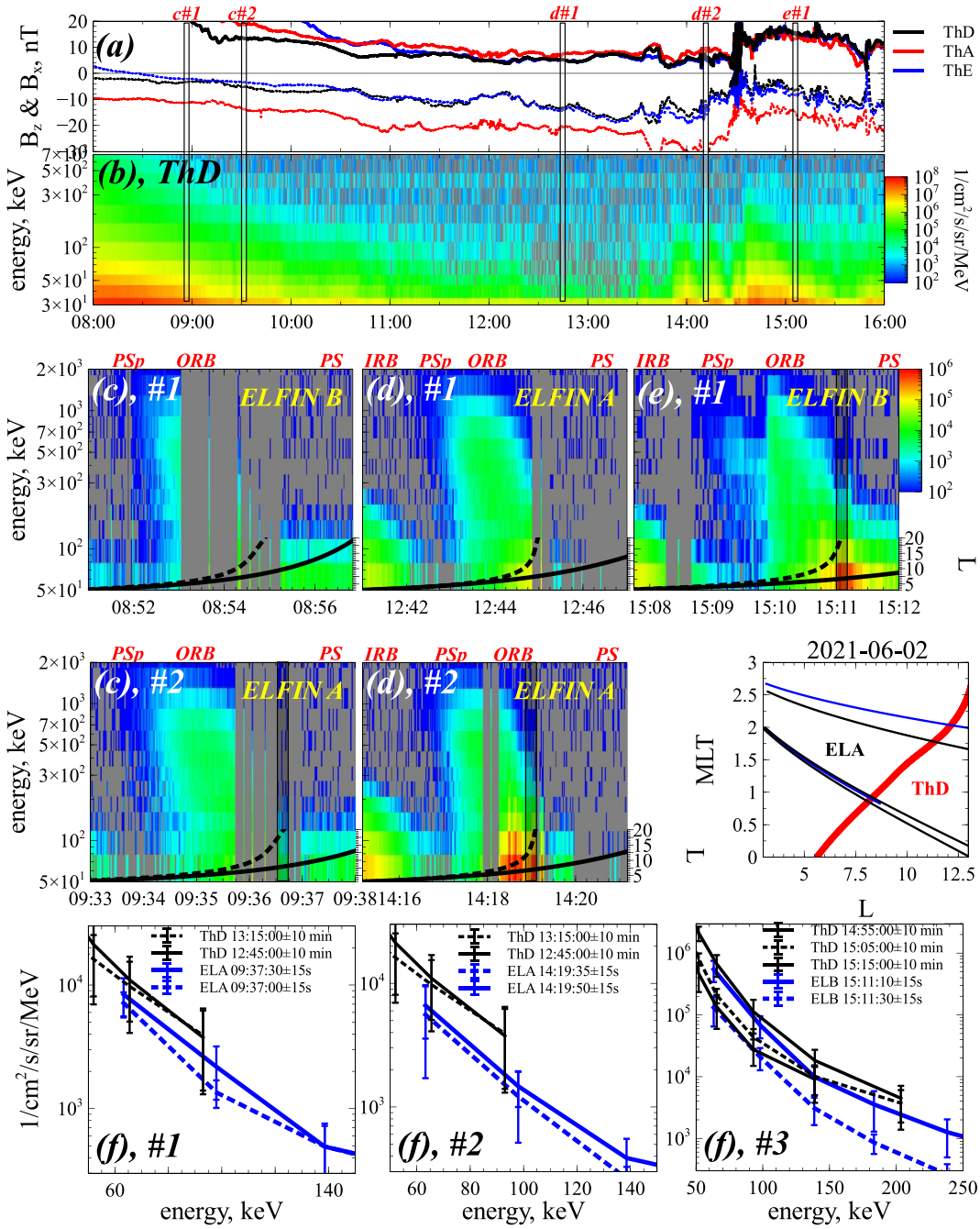

Figure 3. Overview of event #1 from Table 1. Panel (a) shows magnetic field (B_z in solid lines and B_x in dashed lines) for three Time History of Events and Macroscale Interactions during Substorms (THEMIS) spacecraft. Panel (b) shows THEMIS Solid State Telescope electron fluxes at ThD. Panels (c#1, 2), (d#1, 2), and (e#1), show Electron Losses and Fields Investigation (ELFIN) energetic particle detector fluxes during five orbits (International Geophysical Reference System *L* is shown in dotted lines and T89 *L* in solid lines). The gray color in Panels (b), (c#1, 2), (d#1, 2), and (e#1) denotes absence of measurements (times with low count rates can be distinguished from those with lack of measurements by the presence of noise-level counts at >1 MeV). Black boxes in (c#2, d#2, and e#1) show the PS—outer radiation belt interface region. Projections of THEMIS D and ELFIN A, B orbits to the (*L*, magnetic local time (*MLT*)) plane are shown in the bottom right Panel. Panels (f#1–3) compare fluxes from THEMIS and ELFIN during different sub-intervals. Error bars mark the flux dispersion during intervals denoted in the legends.

during current sheet thinning (Panels (d#1, #2)). During these orbits, ELFIN shows the same fluxes in the outer radiation belt (around 12:44 UT and 14:18 UT for ELFIN A) as before 11:00 UT, but a different distribution of energetic electron fluxes at the PS (tailward from the interface region determined for d#2). Around 12:46 UT and 14:20 UT ELFIN A is conjugate to the PS (only <200 keV electron fluxes are measured). ELFIN A measured <200 keV fluxes at about $\sim 10^3 - 10^4$ #/cm^2/s/sr/MeV right after crossing the outer radiation belt boundary (before ~12:45:30 UT and ~14:20 UT, respectively), with almost no fluxes afterward (i.e., in the PS). Comparison of Panels (c#1, #2) and Panels (d#1,# 2), and Panels (f#1) and (f#2) shows that almost the entire PS *shrinks* to lower *L*s (closer to the outer radiation belt). Note that Panel (f#2) does not show ELFIN A fluxes in the PS around 12:46 UT, because the magnitude drops even lower than fluxes around 14:20 UT. After dipolarization, at 15:10 UT, ELFIN B crossed the fully recovered PS with high electron fluxes, $\sim 10^5$ #/cm^2/s/sr/MeV at 63 keV, with detectable fluxes at energies reaching 300 keV (see Panel (e#1), tailward from the interface region). Such high electron fluxes are almost identical to THEMIS D observations in the post-dipolarized PS (~15:00 UT in Panel (b)), that is, $\sim 70 - 200$ keV electrons are well isotropized in the PS and their fluxes are the same around the equator as at low altitudes (see comparison of ELFIN and THEMIS flux distributions in Panel (f#3)).

Figure 4 shows another example of THEMIS and ELFIN observations of the current sheet thinning. The first ELFIN A orbit at ~16:00 UT shows <200 keV electrons in the PS (see Panel (c#1), tailward from the interface region), and the measured flux of $\sim 10^4$ #/cm^2/s/sr/MeV at ~63 keV is quite comparable with flux levels measured at THEMIS, $\sim 10^4 - 10^5$ #/cm^2/s/sr/MeV (even so at ~16:00 UT, when THEMIS E is at some distance from the equator with $B_z \sim |B_x|$). Panel (f#1) compares ELFIN A and THEMIS E fluxes: at 15:59 UT ELFIN A is projected to the PS around THEMIS E location at 16:20 UT (energy spectra measured by both spacecraft are quite close), and at 15:59:20 UT ELFIN A is projected downtail from THEMIS E (ELFIN fluxes are lower than the minimum flux measured at THEMIS E). The current sheet thinning started from ~18:00 UT when THEMIS E was in the PS and started observing a slow B_z decrease without *L* change (B_z decreases with time before ~18:00 UT because THEMIS moves to higher *L*). During the current sheet thinning, ELFIN A crossed the PS twice, at ~19:05 UT and ~20:39 UT (Panels (c#2, d#1), tailward from the interface region). During both crossings, the PS projects to an extremely narrow region at low altitudes: 10 and 3 s respectively, corresponding to 70 and 20 km respectively, or <1° in latitude; beyond this latitudinally narrow region, no energetic electron fluxes were seen. This may be due to the PS being extremely narrow, or extremely cold (such that 50 keV fluxes are negligible) or both. In contrast, ELFIN A and B orbits after the dipolarization (observed at THEMIS at ~22:00 UT) showed a clear PS filled by energetic electrons (Panels (d#2, e#1), tailward from the interface region). At ~22:12:40 UT, ELFIN A crossed the PS and measured a flux of $\sim 10^5$ #/cm^2/s/sr/MeV at ~63 keV, with the energy spectrum very close to the energy spectrum measured by THEMIS E around 22:05 UT (see Panel (f#2), which also shows the range of THEMIS E and ELFIN A flux measurements around the dipolarization). Around ~23:35 UT ELFIN B crossed the PS and measured even higher fluxes at ~63 keV, up to $\sim 10^6$ #/cm^2/s/sr/MeV, and ELFIN energy spectra are again consistent with THEMIS E observations (see Panel (f#3) and compare (b) with (e#1)). Note that variations of energy spectra measured by ELFIN in the PS should be interpreted as a variation of the radial distance of ELFIN projection, whereas the variation of energy spectra measured by THEMIS are due to a combined effect of flux dynamics (correlated with B_z change) and THEMIS projections (correlated with $|B_x|$ change) (see discussions in Gabrielse et al., 2019).

Comparison of near-equatorial (THEMIS) and low-altitude (ELFIN) measurements of energetic electron fluxes, as in Figures 3 and 4, shows the following clear patterns, confirming the previously proposed scenario of the current sheet thinning:

- Prior to current sheet thinning ELFIN observes a distinct PS (extending over several *L*-shells) having flux levels of <200 keV electrons comparable to the near-equatorial fluxes at THEMIS.
- During the current sheet thinning ELFIN shows a latitudinally narrow PS with almost no electron fluxes beyond the outer radiation belt (see the sketch in Figure 5). THEMIS is often far enough from the equator (close to, or even inside the lobe) with barely any electron fluxes, consistent with an extremely thin PS. Whenever THEMIS is at the equator, THEMIS energetic electron flux levels match that of ELFIN at the PS-outer radiation belt interface.
- After dipolarization both ELFIN and THEMIS observe increased fluxes at <200 keV, with comparable levels at the equator and at the low altitudes.

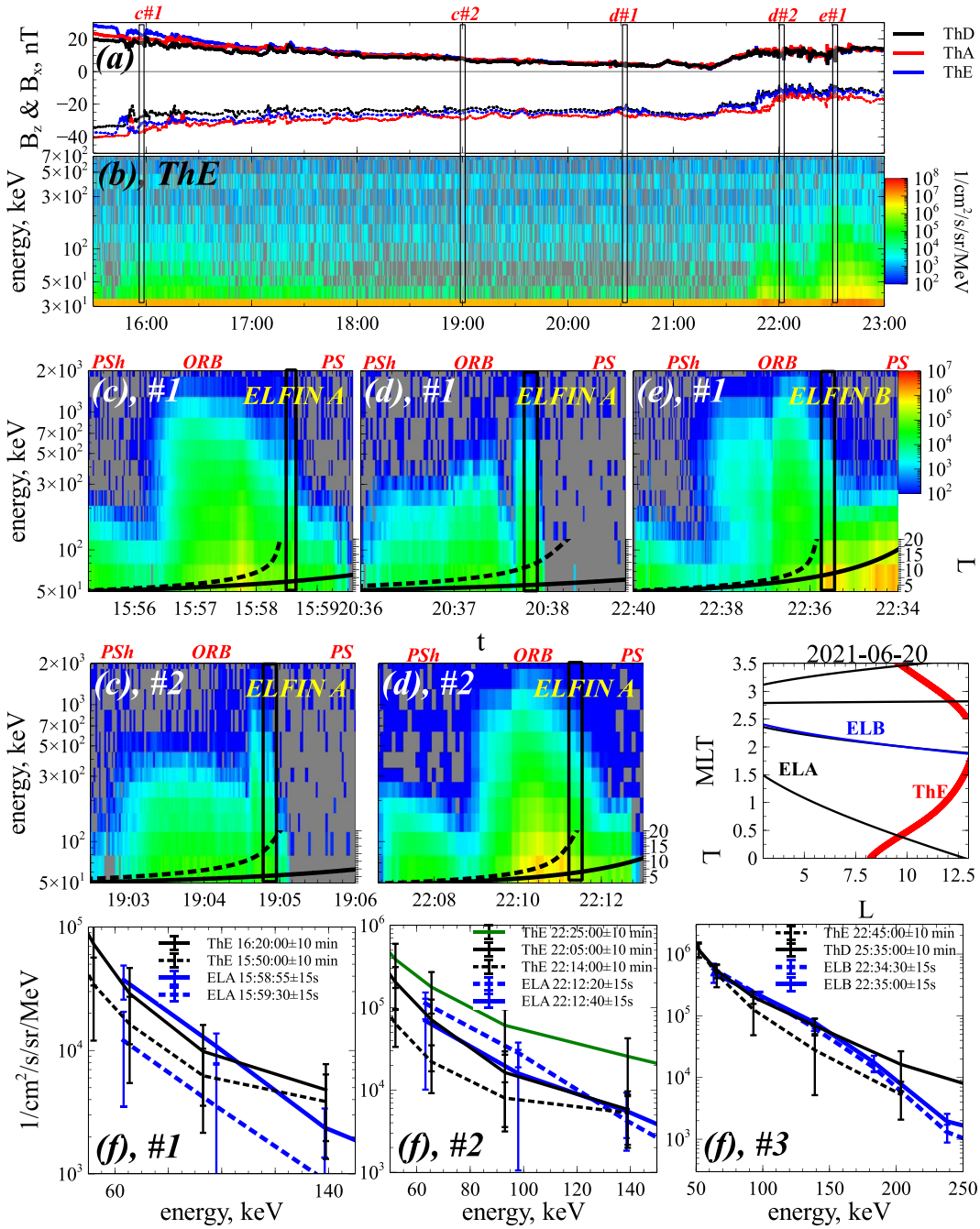

Figure 4. Overview of event #4 from Table 1. Panel (a) shows magnetic field (B_z in solid lines and B_x in dashed lines) for three Time History of Events and Macroscale Interactions during Substorms (THEMIS) spacecraft. Panel (b) shows THEMIS SST electron fluxes at ThE. Panels (c#1, 2), (d#1, 2), and (e#1), show Electron Losses and Fields Investigation (ELFIN) energetic particle detector fluxes during five orbits (International Geophysical Reference System L is shown in dotted lines and T89 L in solid lines). The gray color in Panels (b), (c#1, 2), (d#1, 2), and (e#1) denotes absence of measurements (times with low count rates can be distinguished from those with lack of data by the presence of noise-level counts at > 1 MeV). Black boxes in (c#1, 2, d#1, 2, and e#1) show the PS—outer radiation belt interface region. Projections of THEMIS E and ELFIN A, B orbits to the (L, magnetic local time (MLT)) plane are shown in the bottom right Panel. Panels (f#1–3) compare fluxes from THEMIS and ELFIN during different sub-intervals. Error bars mark the flux dispersion during intervals denoted in the legends.

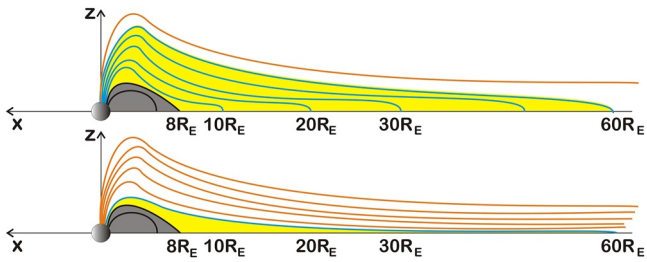

Figure 5. Current sheet reconfiguration during thinning: orange, blue, and black lines show open magnetic field lines, magnetic field lines crossing the PS (yellow), and magnetic field lines of the inner magnetosphere (gray) respectively. Top figure shows quiet time current sheet and bottom figure shows the current sheet at the late thinning stage.

The same pattern of ELFIN/THEMIS energetic electron flux dynamics can be found for all 34 events from Table 1 (see Figures in Supporting Information S1). Similar features for thermal electron (and proton) precipitation during the substorm growth phase have been reported using ground-based observations. Voronkov et al. (1999) demonstrated the narrowing of the latitudinal width of the electron precipitation region, and Wanliss et al. (2000) demonstrated earthward motion of the edge of the PS and proton precipitation region. Such an earthward motion and intensification of PS electron precipitation are often interpreted as signatures of thin current sheet formation near the outer radiation belt edge, that is, at the geostationary orbit (e.g., Kozelova & Kozelov, 2013; Samson et al., 1992). Indeed near-equatorial measurements and simulations have confirm such a combination of stretched magnetic field lines in the middle tail (dB_z/dx decreases at radial distances $>15R_E$ downtail, see Petrukovich et al. (2013); Yue et al. (2015)) and a shrinking in the near-Earth tail (dB_z/dx increases for radial distances $<15R_E$, see Hsieh and Otto (2015); Artemyev, Angelopoulos, Runov, and Petrukovich (2016)). Formation of thin current sheets have been reported at quite-close radial distances, around $6-11R_E$ (Mitchell et al., 1990; Sanny et al., 1994; Sergeev, Mitchell, et al., 1993). Thermal electron (<10 keV) precipitation during the growth phase, however, is largely affected by the presence of field-aligned electrostatic potential drops (e.g., Lessard et al., 2007), whereas our results, based on energetic (>50 keV) electron precipitation, confirm previous ground-based observations at energies that are unaffected by such electrostatic potentials.

3.2. THEMIS, ARTEMIS, MMS, and ELFIN Observations: Radial Distribution of Energetic Fluxes

Figure 6 shows THEMIS, ARTEMIS, and ELFIN observations of the current sheet thinning. The main feature here is that the near-equatorial ARTEMIS P2 satellite (THEMIS C, ThC) shows energetic electron fluxes during the entire interval (Panels (c and d)), and thus we can compare ELFIN's PS flux measurements at the ionosphere with the flux in the mid-tail, $\sim -60R_E$. The current sheet thinning started around 06:00 UT, with the $|B_x|$ increase and B_z decrease at THEMIS (see Panel (a)). The dipolarization interrupting this thinning is associated with a substorm onset (as shown in *AE* index) and appears around 08:20 UT. The manifestation of the same dipolarization (B_z fluctuations and tailward plasma flows of ~ -500 km/s; not shown) is seen by ARTEMIS P2 (ThC) around 08:20-08:40 UT (Panel (c)). THEMIS E and ARTEMIS P2 were near midnight during the entire event: THEMIS E $X \in [-10, -12]R_E$, $Y \in [-1, -4]R_E$ and ARTEMIS P2 $X \sim -59R_E$, $Y \in [-6, -9]R_E$. During the current sheet thinning THEMIS E was around the PS boundary ($|B_x| \sim 20$ nT) and measured an electron flux of $\sim 10^5$ #/cm^2/s/sr/MeV at ~70 keV, whereas after dipolarization ~70 keV electron fluxes reached $\sim 10^6$ #/cm^2/s/sr/MeV (see Panel (b)). During the entire interval, ARTEMIS P2 around the equator measured electron fluxes of $\sim 3 \cdot 10^3$ #/cm^2/s/sr/MeV at ~70 keV (see Panel (d)). Therefore, at $X \in [-12, -60R_E]R_E$ fluxes of ~70 keV electrons are distributed between $5 \cdot 10^3$ and $\sim 10^6$ #/cm^2/s/sr/MeV. The same flux level (between THEMIS and ARTEMIS flux magnitudes) is seen at ELFIN A and B in the PS before the current sheet thinning (after 04:44 UT in Panel (e#1)) and after the dipolarization (09:47 UT in Panel (e#3)): fluxes of 63 keV electrons are the 10^4–10^5 #/cm^2/s/sr/MeV (in Panel (e#1)) and reached $\sim 10^6$ #/cm^2/s/sr/MeV after dipolarization (in Panel (e#3)). Panel (f#1) shows that ELFIN energy spectra are slightly below the THEMIS energy spectra before the thinning (i.e., ELFIN is projected slightly downtail from the THEMIS E location), whereas Panel (f#3) shows that ELFIN and THEMIS energy spectra almost coincide after the dipolarization. Therefore, ELFIN measurements in the PS are generally consistent with near-equatorial THEMIS E and ARTEMIS P2 measurements before the thinning and after dipolarization.

ELFIN A measurements during the current sheet thinning are shown in Figure 6e (#2). There is a very sharp boundary at the interface region with no fluxes of energetic electrons after 07:48:20 UT. This interface region, corresponding to the entire PS encounter by ELFIN-A is ~9 s long (~60 km or ~0.5° in latitude). The PS flux levels measured during these three spins are $\sim 5 \cdot 10^3$ #/cm^2/s/sr/MeV, consistent with levels measured by ARTEMIS P2. Panel (f#2) shows two ELFIN A energy spectra separated by 20 s: the profile at 07:48:10 UT shows that ELFIN is projected earthward from THEMIS, and the profile at 07:48:30 UT shows that ELFIN is projected downtail from ARTEMIS. As both THEMIS E and ARTEMIS P2 measured significant energetic electron fluxes in the magnetotail during the thinning, ELFIN measurements should be interpreted in the context of a magnetic

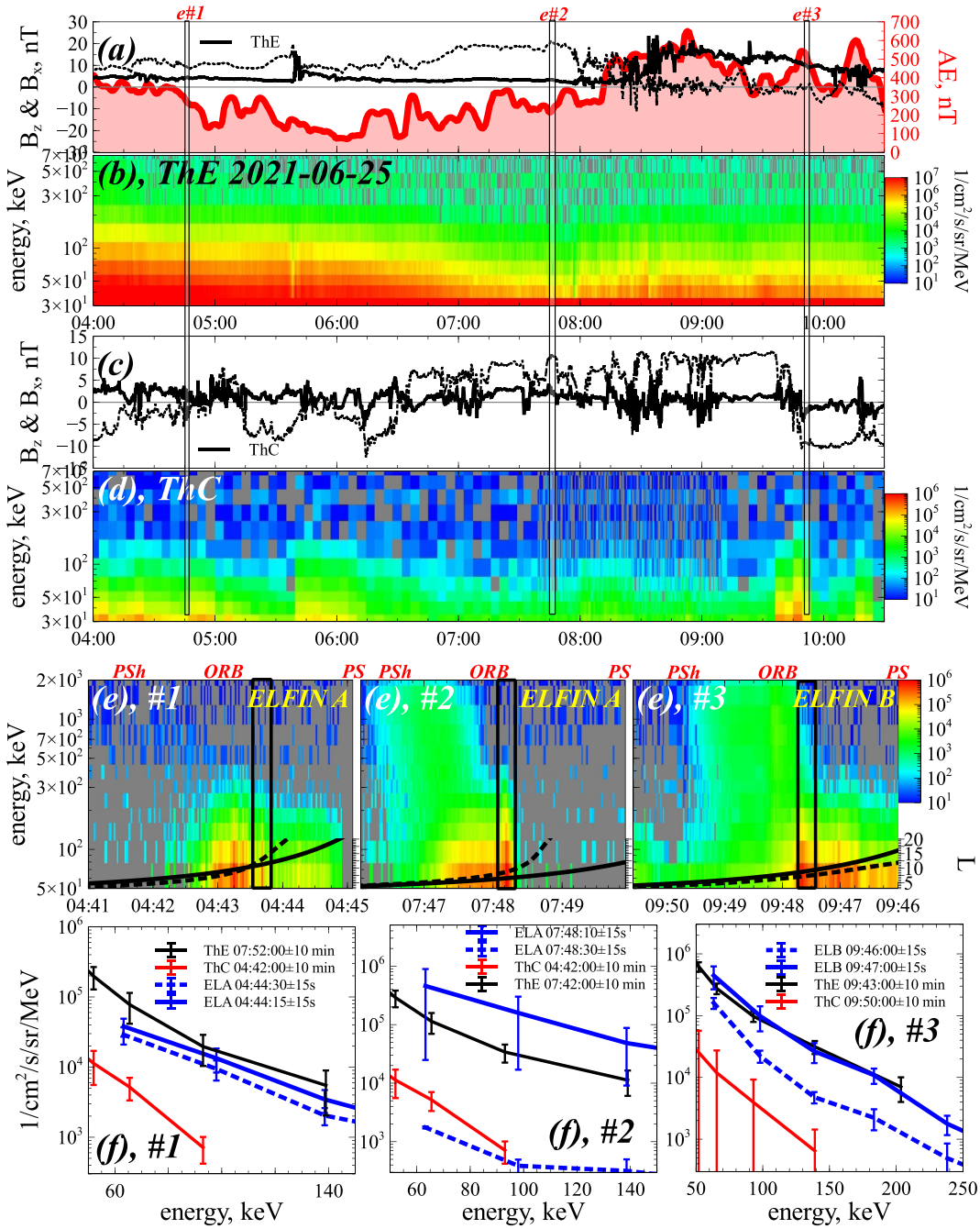

Figure 6. Overview of event #7 from Table 1. Panel (a) shows magnetic field (B_z, solid line; B_x, dashed line) for ThE, and the Time History of Events and Macroscale Interactions during Substorms (THEMIS) AE index (derived from THEMIS ground based and ancillary magnetometers around the world). Panel (b) shows SST electron fluxes at THEMIS E. Panel (c) shows magnetic field (B_z in solid line and B_x in dashed line) for Acceleration, Reconnection, Turbulence and Electrodynamics of the Moon's Interaction with the Sun (ARTEMIS) P2 (THEMIS C). Panel (d) shows ARTEMIS SST electron fluxes for P2 (ThC). Panels (e#1–3) show Electron Losses and Fields Investigation (ELFIN) energetic particle detector fluxes during three orbits (IGFR L is shown in dotted lines and T89 L in solid lines). The gray color in Panels (b), (e#1–3) denotes absence of measurements, whereas black boxes show the PS—outer radiation belt interface region. Panels (f#1–3) compare fluxes from THEMIS, ARTEMIS, and ELFIN during different sub-intervals. Error bars mark the flux dispersion during intervals denoted in the legends.

field reconfiguration. The current sheet thinning stretches magnetic field lines crossing the PS, but groups them into a dense bunch at the inner edge of the PS. So the entire PS from its transition region all the way to the lunar orbit at $\sim 60R_E$ is mapped to only a couple of degrees in magnetic latitude traversed by ELFIN right after the outer radiation belt during a few spins (at or adjacent to the interface region). The entire PS is seen by ELFIN A between 07:48:10-07:48:20 UT. Indeed, the contrast between Panels (e#1, 3) and Panel (e#2) is well seen: there is no large-scale (spanning more than several magnetic latitude degrees) PS at low altitudes during the current sheet thinning.

Figure 7 shows THEMIS, MMS, and ELFIN observations of the current sheet thinning, that is, the situation is similar to that of Figure 6, but instead of $X \approx -60R_E$ ARTEMIS measurements we use $X \approx -27R_E$ MMS measurements. The current sheet thinning starts around 02:30 UT, with $|B_x|$ increase and B_z decrease seen by both THEMIS E and MMS (see Panels (a and d)). There are several small-scale injections before the substorm onset and dipolarization around 05:50 UT (best seen in THEMIS E B_z and AE index; Panel (a)). Before the current sheet thinning, around 02:00 UT, THEMIS E and MMS measure an electron flux of $\sim 10^5 - 10^6$ #/cm^2/s/sr/MeV at ~70 keV, with MMS fluxes smaller than THEMIS fluxes due to their difference in radial distances. The current sheet thinning is associated with THEMIS E and MMS apparent *motion* toward the PS boundary (we interpret the observed $|B_x|$ increase as current sheet thinning and associated reduction in current sheet thickness, L_{CS}, hence an increase in the relative distance, z/L_{CS}, of the satellite from the neutral sheet) and ~70 keV electron fluxes go to $\sim 10^4$ #/cm^2/s/sr/MeV at THEMIS E around 03:30 UT and on MMS around 04:00 UT. The flux increase at the dipolarization is better seen at THEMIS where ~70 keV electron fluxes exceed $\sim 10^7$ #/cm^2/s/sr/MeV around 05:50UT. Therefore, the range of ~70 keV electron flux variations (between $[-10, -30]R_E$) during the entire interval is from $\sim 3 \cdot 10^3$ #/cm^2/s/sr/MeV (note that THEMIS E and MMS $|B_x|$ indicate that this flux magnitude maps to the middle/deep magnetotail) to $\sim 10^6$ #/cm^2/s/sr/MeV.

Before the current sheet thinning and after dipolarization, ELFIN A (Panel (e#1)) and B (Panel (e#5)) made a prolonged traversal of the PS with $\leq 10^5$ #/cm^2/s/sr/MeV fluxes of ~63 keV electrons tailward of the interface region; comparable to MMS measurements. ELFIN A, B measure even $\sim 10^7$ #/cm^2/s/sr/MeV fluxes around the outer radiation belt boundary (~01:12:10 UT in Panel (e#1) and ~07:00:10 UT in Panel (e#5)). Therefore, THEMIS E (at near Earth) and MMS (at middle tail) flux measurements are in agreement with ELFIN A, B fluxes in the PS region.

During the current sheet thinning ELFIN B measurements (see Panels (e#3, 4)) show the formation of a sharp boundary at the interface region right at the outer radiation belt edge. An interesting difference with events shown in Figures 3–6 is that detectable fluxes of ~63 keV electrons (and even ~100 keV electrons) occupy a wide latitudinal range associated with the PS. The substrom thinning process did not reconfigure the current sheet sufficiently to shrink it to a few degrees around the outer radiation belt edge at low altitudes, but PS fluxes outside a narrow interface region decreased significantly. Fluxes of ~63 keV electrons in the PS (e.g., before 03:54 UT in Panel (e#3) and before 05:27 UT in Panel (e#4); note that time is reversed for these Panels to show the PS to the right) are well below 10^4 #/cm^2/s/sr/MeV, that is, below THEMIS and MMS fluxes. Thus, outside a few ELFIN spins within the interface region, ELFIN is projected to radial distances much larger than MMS location, and almost the entire PS seen by THEMIS E and MMS (between $-10R_E$ and $-30R_E$) shrinks to these few ELFIN spins.

Figure 8 compares energy spectra from five ELFIN orbits and from THEMIS, MMS during the event from Figure 7. Panel (a) shows ELFIN A measurements before the current sheet thinning: at 01:10:45 UT, ELFIN A is projected to the equatorial region around MMS and THEMIS measurements (note THEMIS $|B_x| > 20$ nT and thus THEMIS measured electron fluxes coming from the downtail region). At 1:10:00 UT ELFIN A is projected earthward from the THEMIS and MMS location, and electron fluxes at ELFIN are higher than fluxes measured by the near-equatorial spacecraft. Panel (b) shows ELFIN B measurements during the current sheet thinning: ELFIN B fluxes at 02:19:45 UT are below MMS fluxes (i.e., ELFIN is projected downtail from MMS location), fluxes at 02:20:30 UT are comparable to MMS fluxes, and fluxed at 02:20:50 UT are slightly below THEMIS fluxes. Such strong variations of ELFIN B fluxes is typical for the current sheet thinning interval, when the entire PS shrinks significantly. Panel (c) further confirms such shrinking: at 03:53:25 UT ELFIN B measured fluxes almost identical to near-Earth PS fluxes from THEMIS E, whereas at 03:53:10 UT ELFIN B measured fluxes very similar to the smallest MMS fluxes (note that MMS at this moment captures $|B_x| > 10$ nT and thus MMS measured electron fluxes further downtail from its equatorial position, i.e., at radial distance above $30R_E$). Therefore, within 15 s,

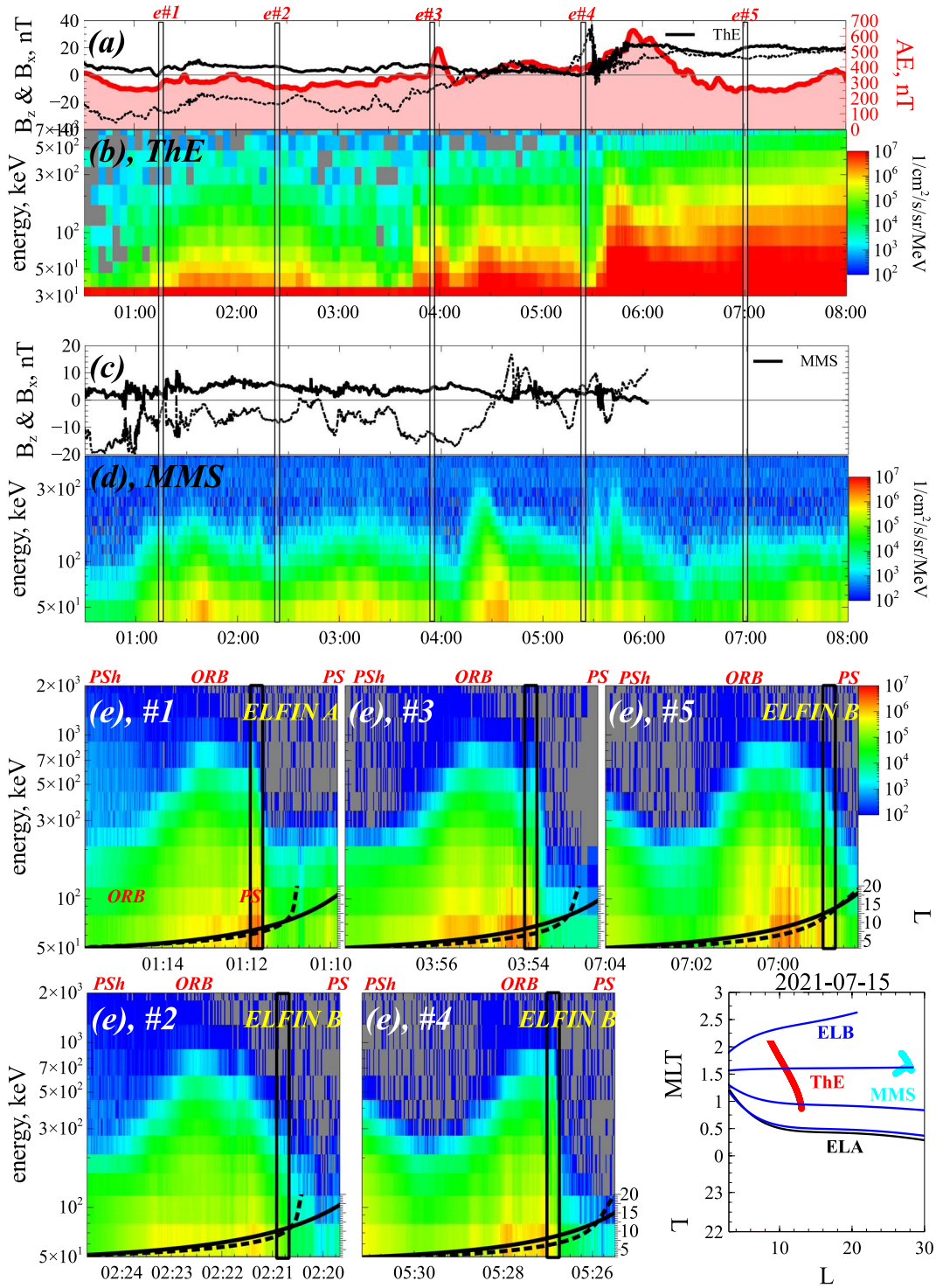

Figure 7. Overview of event #17 from Table 1. Panel (a) shows magnetic field (B_z in the solid line and B_x in the dashed line) for ThE, and Time History of Events and Macroscale Interactions during Substorms (THEMIS) AE index. Panel (b) shows SST electron fluxes for THEMIS E. Panel (c) shows magnetic field (B_z in the solid line and B_x in the dashed line) for Magnetospheric Multiscale Mission (MMS)#1. Panel (d) MMS #1 Fly's Eye Energetic Particle Spectrometer electron fluxes. Panels (e#1–5) show Electron Losses and Fields Investigation (ELFIN) energetic particle detector fluxes during five orbits (International Geophysical Reference System *L* is shown in dotted lines and T89 *L* in solid lines). Black boxes in (e#1–5) show the PS—outer radiation belt interface region. Projections of THEMIS E, MMS#1 and ELFIN A, B orbits in the (*L*, magnetic local time (*MLT*)) plane are shown in the bottom right Panel.

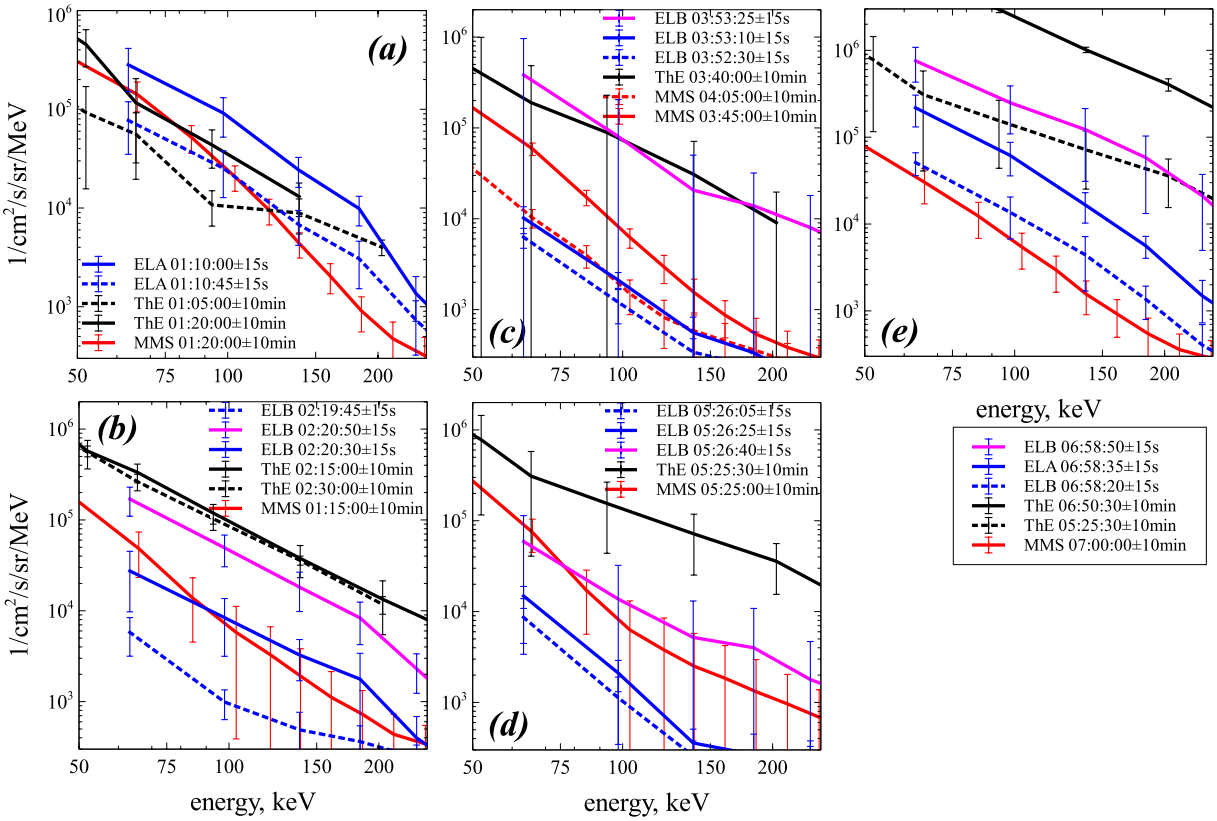

Figure 8. Fluxes from Time History of Events and Macroscale Interactions during Substorms, Magnetospheric Multiscale Mission (MMS), and Electron Losses and Fields Investigation during the event shown in Figure 7. Error bars mark the flux dispersion during intervals denoted in the legends.

ELFIN crossed field lines projected from $10R_E$ to $>30R_E$. Right before the substrom onset (at 05:30 UT), ELFIN B crossed the thinnest current sheet. Panel (d) shows that ELFIN B fluxes right after the transition region (at 05:26:40 UT) are very close to MMS fluxes measured at $\sim 30R_E$, whereas 15 s before (at 05:26:25 UT) ELFIN B measured fluxes much lower than the MMS flux magnitude, that is, ELFIN B is projected downtail from MMS location. Panel (e) shows ELFIN B measurements after dipolarization (after the substorm onset): ELFIN fluxes are distributed between near-Earth THEMIS E measurements (at 05:25 UT, before THEMIS E approached the Earth) and MMS fluxes measured at 07:00 UT. Therefore Figure 8 demonstrates how ELFIN projections to the equatorial PS changes during the entire substorm cycle.

Comparison of Figures 6 and 7 shows that strong PS flux variations during the current sheet thinning do not always result in the PS shrinking to a few ELFIN spins at low-altitude measurements. Although the near-Earth PS does shrink to the narrow interface region in both events, in Figure 7 ELFIN still measured energetic electron fluxes from the deep tail (further downtail from MMS) outside this narrow layer. Our database (see Supporting Information S1) has been collected without any restrictions on ELFIN flux measurements, but only with the requirement of THEMIS observations of current sheet thinning. Therefore, this data set contains events with various levels of low latitude electron fluxes in the PS during the current sheet thinning. However, for all events we observe the same trend of strong decrease of these fluxes outside a narrow interface region (a few ELFIN spins) attached to the outer radiation belt boundary. Comparison of ELFIN fluxes with ARTEMIS and MMS fluxes shows that only a few spins away from the radiation belt boundary ELFIN may measure fluxes from the deep magnetotail (beyond the ARTEMIS orbit) or even cross open magnetic field lines without energetic electrons, that is, ELFIN projection right outside the radiation belt boundary may trace the near-Earth PS (before the current sheet thinning or after dipolarization) and deep magnetotail (during the current sheet thinning). These results are well seen in Figures 6 and 7 and can be derived for events #14, 16, 22, 24–26, 31, 33 from Table 1 (see figures for these events in Supporting Information S1).

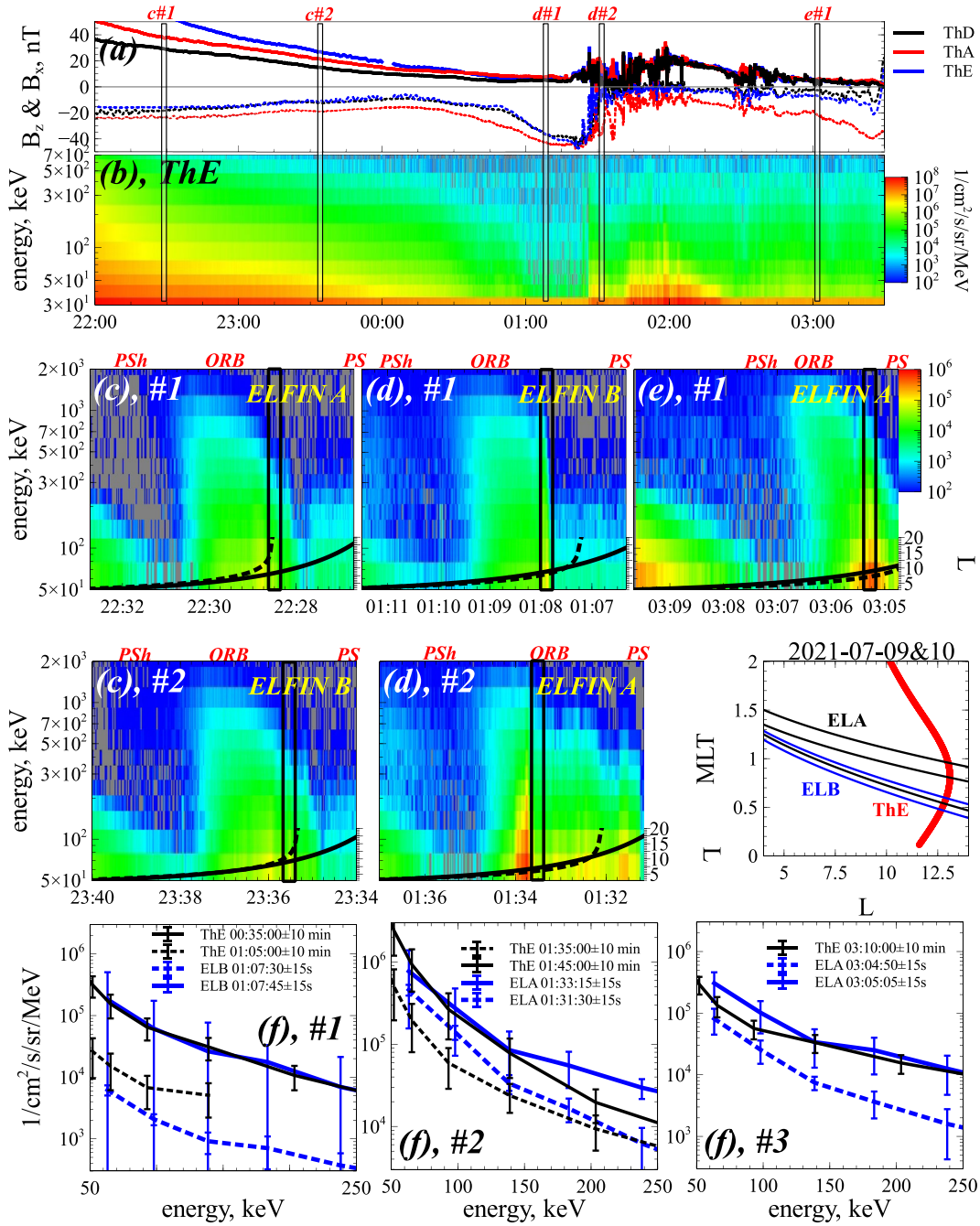

Figure 9. Overview of event #13 from the table in the main text. Panel (a) shows magnetic field (B_z in solid lines and B_x in dashed lines) for three Time History of Events and Macroscale Interactions during Substorms (THEMIS) spacecraft. Panel (b) shows SST electron fluxes for THEMIS E. Panels (c#1, 2), (d#1, 2), and (e#1), show Electron Losses and Fields Investigation (ELFIN) energetic particle detector fluxes during five orbits (International Geophysical Reference System L is shown in dotted lines and T89 L in solid lines). Black boxes in (c#1,2, d#1,2, and e#1) show the PS—outer radiation belt interface region. Projections of THEMIS E and ELFIN A, B orbits to the (L, magnetic local time (MLT)) plane are shown in the bottom right Panel. Panels (f#1–3) compare fluxes from THEMIS and ELFIN during different sub-intervals. Error bars mark the flux dispersion during intervals denoted in the legends.

3.3. THEMIS and ELFIN Observations: Time-Scale of CS Reconfiguration

Figure 9 shows a typical event of THEMIS and ELFIN observations of the current sheet thinning, but constrast to events from Figures 3–6 PS electron fluxes at low altitudes do not decrease to zero and remain very small, but finite during the current sheet thinning (like in event from Figure 7). An interesting feature of this event is that

two ELFIN orbits before and after dioporization are separated by only 25 min. The current sheet thinning started around 00:00 UT and ended by a dipolarization at 01:30 UT (see Panel (a)). There are very clear signatures of fast formation of thin current sheet ($|B_x|$ increases from 20 to 40 nT within 1 hr), and this thinning *moves* the spacecraft to the PS boundary with the ~70 keV electron flux decreasing from 10^7 #/cm^2/s/sr/MeV around 00:00 UT down to the noise level $<10^4$ #/cm^2/s/sr/MeV around 01:20 UT. ELFIN A and B crossings of the PS show that before the current sheet thinning ~63 keV electron fluxes are ~10^4 #/cm^2/s/sr/MeV (see Panels (c#1) around 22:27:30 UT and (c#2) around 23:34:30 UT, tailward from the interface region). During the current sheet thinning ELFIN B observed the formation of a very sharp boundary with the interface region (around 01:07:55 UT in Panel (d#1)), whereas tailward from the interface region the PS fluxes of ~63 keV electrons decreased below ~10^3 #/cm^2/s/sr/MeV (but remains finite). Panel (f#1) shows that ELFIN B energy spectrum at 01:07:45 UT coincides with the THEMIS E energy spectrum before the thinning, whereas at 01:07:30 UT ELFIN B energy spectrum is below the minimum THEMIS E fluxes at 01:05 UT (note THEMIS $|B_x|$~ 40 nT at this moment and hence is projected to an equatorial position well downtail). The next ELFIN A orbit crossed the PS right during the dipolarization, around 01:34UT. ELFIN A observed significant increase of the ~63 keV electron fluxes reaching 10^6 #/cm^2/s/sr/MeV and expansion of the energy range of the PS electrons up to 1 MeV (see Panel (d#2), poleward from the interface region). These observations are consistent with THEMIS E observations around 01:30-01:40 UT, when $|B_x|$ decreased to almost zero, B_z significantly increased and was oscillating, while ~70 keV electron fluxes reached ~$10^6 - 10^7$ #/cm^2/s/sr/MeV. Panels (f#2,3) confirm that ELFIN A energy spectra after the dipolarization are very close to THEMIS E energy spectrameasured in the near-Earth PS. Therefore, a near-equatorial reconfiguration of the magnetotail PS within ~15 min of the dipolarization was observed at ELFIN's energetic electron fluxes.

Figure 10 shows an event with the current sheet thinning and dipolarization observed by ELFIN A and B orbits with only a 10-min separation. The current sheet thinning starts around 21:30 UT and ends by a dipolarization around 22:40 UT. There is an additional dipolarization latter, around 00:00 UT, but we restrict our analysis to 19:00-23:00 UT. Before the current sheet thinning, around 19:40 UT, THEMIS D and ELFIN A observed the PS with ~70 keV electron fluxes of ~10^4 #/cm^2/s/sr/MeV at THEMIS (see Panel (b)) and ~$10^3 - 10^4$ #/cm^2/s/sr/MeV at ELFIN A (see Panel (c#1), 19:42 UT, tailward from the interface region). Panel (f#1) confirms that ELFIN A and THEMIS D energy spectra are quite close to each other during ELFIN's crossing of the interface region, whereas ELFIN A fluxes are much smaller then THEMIS D fluxes when ELFIN A is projected downtail from THEMIS D. The current sheet thinning *moves* THEMIS D to the boundary of the PS without energetic electrons (around 21:45 UT), but a small injection at ~21:55 UT changes the PS configuration (as seen from the B_x change) and *returns* THEMIS D closer to the equator. Thus, before the main injection at 22:45 UT, THEMIS D observed ~70 keV electron fluxes of ~10^5 #/cm^2/s/sr/MeV, and these fluxes increased to ~10^6 #/cm^2/s/sr/MeV after the injection. Note that during the entire interval the THEMIS spacecraft were quite close to the Earth, at $L < 10$. Comparison of ELFIN A and B orbits around the injection (Panels (c#1) and (d#1)) shows a dramatic change of the PS electron fluxes within a few minutes. Around 22:47:30 UT ELFIN A did not see an extended PS and all electron fluxes in the PS were observed within the interface region of a few ELFIN spins (between 22:46:40 UT and 22:46:55 UT), that is, the PS projection to low altitudes shrunk and moved to the outer radiation belt edge. Around 22:56 UT, however, ELFIN B observed a prolonged PS filled by energetic (<300 keV) electrons with fluxes comparable to the equatorial THEMIS D measurements, that is, ~63 keV electron flux around 22:56:30 UT reaches ~10^6 #/cm^2/s/sr/MeV. As shown in Panels (f#2, 3), right before the dipolarization and after dipolarization ELFIN A,B energy spectra nearby of the interface region are very close to the THEMIS D energy spectra, whereas before the dipolarization Panel (c#2) shows no fluxes at ELFIN A beyond the narrow layer around the interface region. Compassion of panels (f#2, 3) and (c#2, d#1) underlines significant changes of the PS projection to low altitudes during ~10 min, with an almost unchanged projection of the narrow layer around the interface between the PS and inner magnetosphere.

Figures 9 and 10 demonstrate that the magnetic field reconfiguration during the dipolarization in the equatorial magnetotail takes less than 20 min, and within this interval the latitudinal extent of the low-altitude projection of the PS (or equivalently the *L*-shell extent) may rapidly change. These observations supplement results about ELFIN observations of the PS shrinking during the equatorial current sheet thinning.

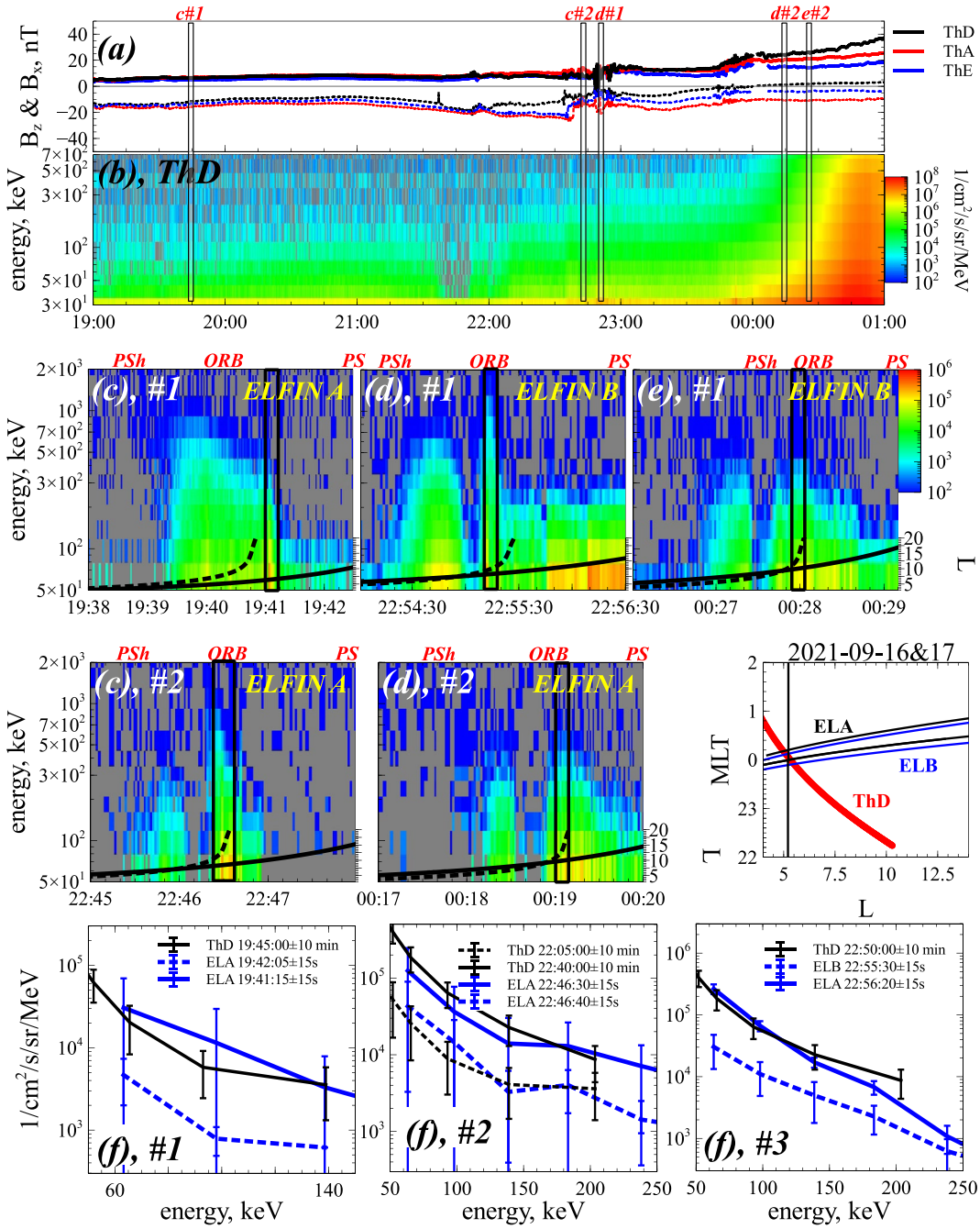

Figure 10. Overview of event #32 from the table in the main text. Panel (a) shows magnetic field (B_z in solid lines and B_x in dashed lines) for three Time History of Events and Macroscale Interactions during Substorms (THEMIS) spacecraft. Panel (b) shows SST electron fluxes for THEMIS D. Panels (c#1, 2), (d#1, 2), and (e#1), show Electron Losses and Fields Investigation (ELFIN) energetic particle detector fluxes during five orbits (International Geophysical Reference System *L* is shown in dotted lines and T89 *L* in solid lines). Black boxes in (c#1, 2, d#1,2, and e#1) show the PS—outer radiation belt interface region. Projections of THEMIS D and ELFIN A orbits to the (*L*, magnetic local time (*MLT*)) plane are shown in the bottom right Panel. Panels (f#1–3) compare fluxes from THEMIS and ELFIN during different sub-intervals. Error bars mark the flux dispersion during intervals denoted in the legends.

4. Statistics

To statistically compare THEMIS and ELFIN flux measurements, we combine all ELFIN orbits during events in Table 1. Figures 11a and 11b shows the distribution of measurements (number of spins with valid electron measurements) in the (*MLT*, *L*) space. Note that the results in Figure 11 are based on all ELFIN and THEMIS

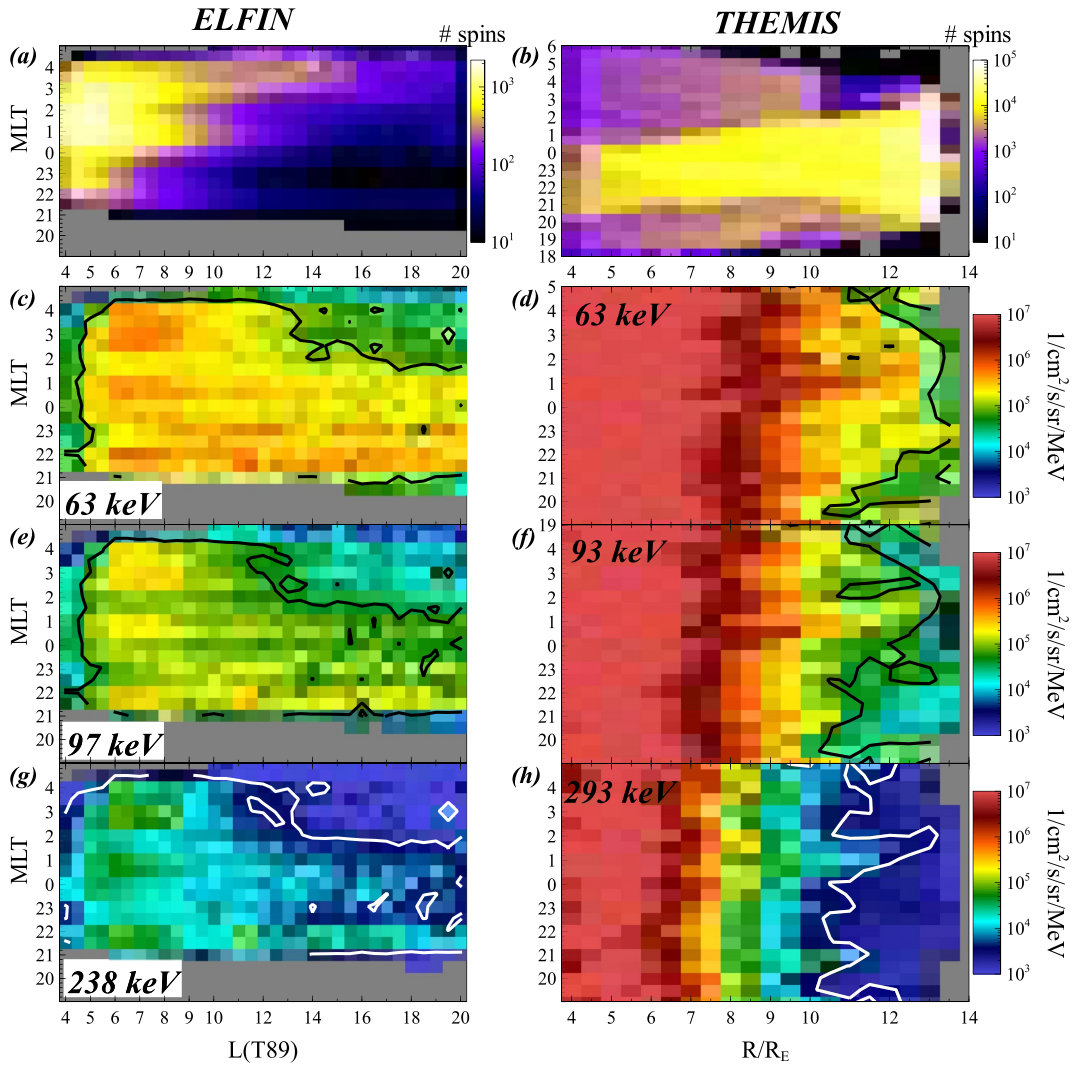

Figure 11. Statistics of Time History of Events and Macroscale Interactions during Substorms (THEMIS) and Electron Losses and Fields Investigation (ELFIN) measurements for all events in Table 1. Panel (a) shows number of spins (number of electron spectra) measured by ELFIN in the (magnetic local time (*MLT*), *L*) plane. Panel (b) shows the same spin number distribution for THEMIS in the (*MLT*, r/R_E) plane. Panels (c–h) show the average ELFIN and THEMIS fluxes for three typical energies of energetic PS electrons.

measurements in conjunction, independent of timing relative to the dipolarization. For the time interval with conjugate THEMIS and ELFIN measurements (June–September 2021), most of ELFIN measurements are within $MLT \in [23, 04]$ and most of THEMIS measurements are within $MLT \in [20, 03]$. THEMIS spacecraft cover the radial distance (evaluated with T89 model (Tsyganenko, 1989)) down to $13R_E$, whereas ELFIN IGRF *L*-shell is not so meaningful due to uncertainties of field-line projections outside the inner magnetosphere. Comparison of ELFIN and THEMIS fluxes (Figures 11c–11h) shows two main trends:

- There is a peak of ELFIN fluxes around the outer radiation belt, $L \in [5, 8]$ (clearly seen in the 238 keV channel); in the PS ($L > 9$), fluxes do not depend on *L* because of large uncertainties of *L* in the PS. These PS ELFIN fluxes are about the same as THEMIS equatorial fluxes in the near-Earth PS, $r \in [10, 12]R_E$. Therefore, we confirm that statistically the fluxes of energetic electrons measured by ELFIN and THEMIS in the PS are quite similar, that is, these electron populations are well isotropized.
- A transition between isotropic (having similar magnitudes on THEMIS and ELFIN) and strongly anisotropic (having much larger magnitudes at THEMIS than on ELFIN) fluxes occurs around $r \sim 9R_E$: for $r < 9R_E$

equatorial electron fluxes are much larger than ELFIN fluxes in the radiation belts. Therefore, we should expect to observe the radiation belt—PS interface at the edge of the outer radiation belt, ~$9R_E$.

- The radial distance below which THEMIS fluxes exceed those at ELFIN decreases from $10R_E$ to $8R_E$ as the energy increases from ~63 keV to ~250 keV. This can be understood in terms of isotropization due to field-line scattering: larger energies may be scattered by stronger equatorial field and larger equatorial curvature radius (Delcourt et al., 1994, 1996; Sergeev et al., 1983), which occurs closer to Earth. Field-line scattering at larger distances is therefore consistent with the observed pitch-angle isotropization of the electrons leading to similar trapped fluxes observed at ELFIN (corresponding to low equatorial pitch-angles) and THEMIS (dominated by large equatorial pitch angles).

Next, we combine all ELFIN measurements during the 34 events in Supporting Information S1 and bin them into three groups (using simultaneous THEMIS measurements in the PS): pre-thinning (before the current sheet thinning), the growth phase (during the current sheet thinning), and the expansion phase (after dipolarization observed by THEMIS). For each ELFIN orbit we determine the moment t_0 at middle of the interface region, and use the interface region width of ±6s (i.e., two spins) from t_0. We also determine the moment (t_L) of crossing a lower L boundary, as a boundary between the outer radiation belt and the plasmasphere (the region filled by >500 keV electrons with a gap in <500 keV electron fluxes on ELFIN). The moment (t_M) of crossing a larger L boundary is determined by the end of ELFIN measurements on the PS side. Then we shift the time for each orbit as $t - t_0$. Intervals $t_L - t_0$ and $t_M - t_0$ are normalized to their duration. Thus, for each orbit we have a new time from −1 to 0 (the outer radiation belt region), and from 0 to + 1 (the PS region). Figure 12 (Panels (a and b)) shows such ELFIN measurements with rescaled times that are further categorized into three epoch analysis (*time*, *energy*) distributions. There are clear differences of electron fluxes in the PS (epoch time >0) for the three data subsets. This difference is seen even better in Panels (c) plotted versus magnetic latitude *MLat* (centered to the time moment t_0, but without *MLat* rescaling).

To confirm the categorization of ELFIN orbits into three groups, we also calculate magnetic field components measured by THEMIS spacecrafts in the PS (only measurements at $r > 9R_E$ are used) during ELFIN crossings of the PS (±10 min). The bottom Panel in Figure 12 shows distributions of $\langle B_{xy}\rangle = \sqrt{\langle B_x\rangle^2 + \langle B_y\rangle^2}$, $\langle B_z\rangle$ during three groups of ELFIN orbits. For the *pre-thinning* group, THEMIS B_z is about ∈ [5, 20]nT, typical of a quiet, near-Earth PS (see, e.g., Artemyev et al., 2013). The magnitude of B_{xy} ∈ [10, 40] nT depends on the distance of THEMIS from the current sheet center (B_x, B_y reversals at the equator); for the *pre-thinning* group we have B_{xy}/B_z ∈ [1, 10], which are also quite typical values of the magnetic field ratio in the near-Earth current sheet (e.g., Artemyev, Angelopoulos, & Runov, 2016). For the *growth phase* group, the B_z distribution shows an expected B_z decrease to the range ∈ [3, 10]nT. Due to the current sheet thinning THEMIS spacecraft appear at the PS boundary with larger B_{xy} ∈ [20, 50] nT. For the *expansion phase* group, B_z increases due to dipolarization up to ∈ [5, 20]nT, and the PS expansion (the thin current sheet destruction) results in smaller B_{xy} at THEMIS, B_{xy} ∈ [5, 40] nT (there are much more observations with $B_z/B_{xy} \sim 1$ during the *expansion phase* in comparison with the *growth phase*).

The top Panels of Figure 12 show a significant drop of energetic electron fluxes in the PS (epoch time >0 and $\Delta MLat > 0$) during the *growth phase*, compared to the *pre-thinning*. Moreover, there are fewer measurements above the noise level at all electron energies in the PS during the *growth phase* (see middle Panels of Figure 12). The *expansion phase* is characterized by very high fluxes and higher electron energies in the PS.

Therefore, Figure 12 statistically confirms the main results from the above case studies: during the current sheet thinning, almost the entire PS at low altitudes (as shown by energetic electrons) shrinks to a small interface region adjacent to the outer radiation belt edge. This is purely an effect of the magnetic field line projection during the substorm growth phase, because near-equatorial THEMIS, MMS, and even ARTEMIS spacecraft still observe energetic (~63 keV and above) electrons around the B_x reversal (i.e., near the equator) during the current sheet thinning at levels detectable by ELFIN (see Figures 3–10 and Supporting Information S1). Moreover, Figure 12 (c) further shows that during the current sheet thinning the flux magnitudes similar to the pre-thinning level can be measured within the interface region of $|MLat| < 2°$ (for >50% of observations, see panel (b)), that is, this statistical picture confirms the scenario of the PS shrinking into a very narrow interface region.

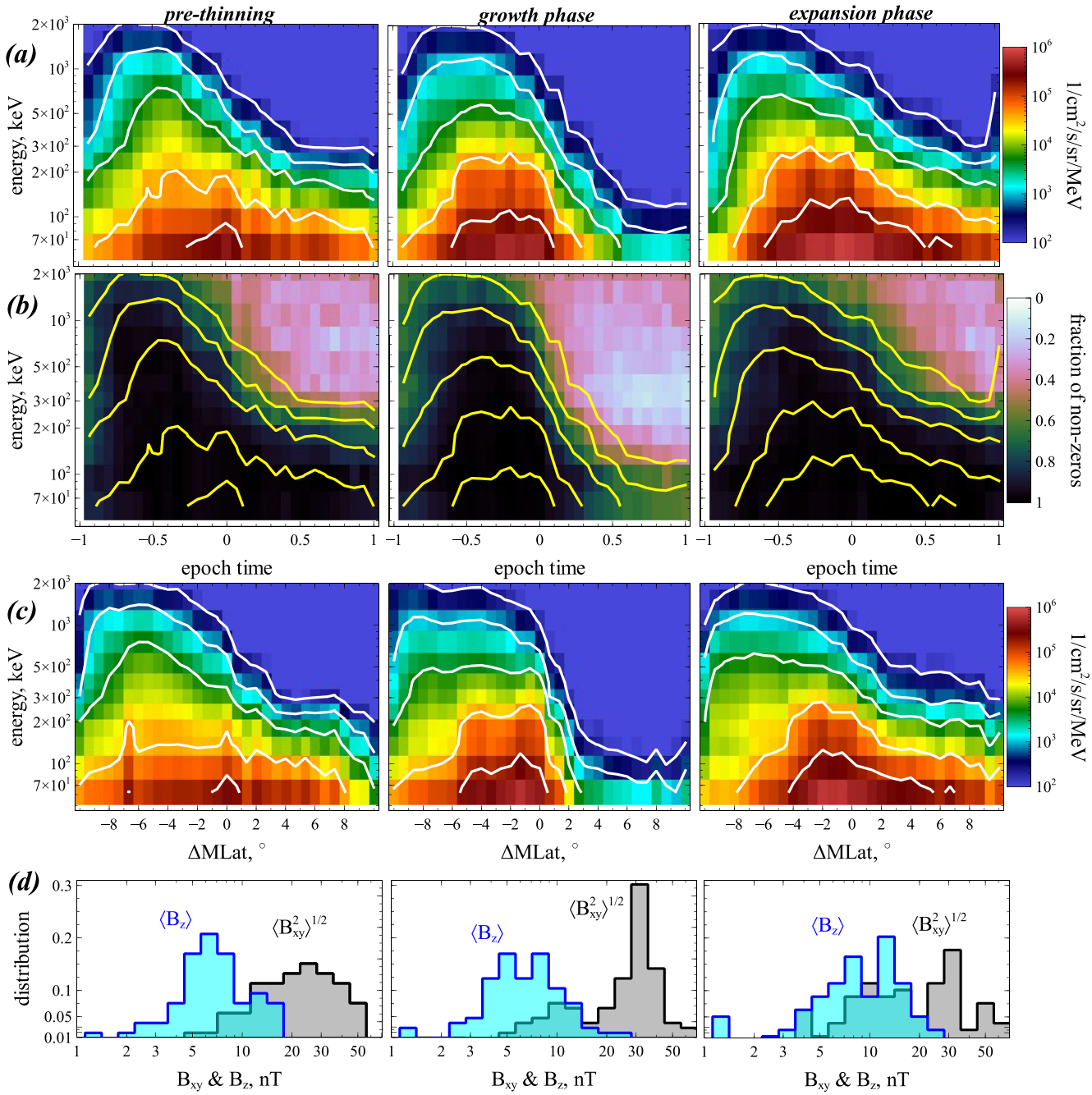

Figure 12. Superposed epoch analysis of Electron Losses and Fields Investigation (ELFIN) flux measurements during the 34 events presented in Supporting Information S1. Panels (a) show electron fluxes with rescaled epoch time, where $t = 0$ is the mid-point of the radiation belt ($t < 0$)—PS ($t > 0$) interface; see text for details. Panels (b) show percentage of number of spins with ELFIN flux measurements above the noise level. Panels (c) show electron fluxes versus centered magnetic latitude, where $MLat = 0$ means the boundary between the outer radiation belt ($\Delta MLat < 0$) and PS ($\Delta MLat > 0$). Panels (d) show distributions of magnetic fields measured by Time History of Events and Macroscale Interactions during Substorms during ±10 min around ELFIN orbits (see text for details).

5. Discussion and Conclusions

In this study we examine the dynamics of the PS as traced by energetic electrons at low altitudes. Electrons of energy ∈[50, 200] keV move very quickly and low-altitude measurements can be used as snapshots of the PS radial profile of such electron fluxes. Using simultaneous measurements at ELFIN (at ~450 km altitude) and

at the equatorial THEMIS, MMS, and ARTEMIS spacecraft during the current sheet thinning process we have shown:

1. In the quiet PS, the equatorial and low-altitude fluxes of [50, 200] keV electrons are very similar both in magnitudes and energy spectra, that is, equatorial energetic electron fluxes are isotropic. The PS occupies a large range of latitudes (large range of radial distances) at low altitudes. The current sheet thinning (associated with the substorm growth phase as determined by THEMIS observations of a B_z decrease and $|B_x|$ increase) is characterized by a significant shrinking of the PS mapped to low altitudes: ELFIN measurements of energetic electron fluxes outside the outer radiation belt are limited to a few seconds (a couple of magnetic latitude degrees). We interpret these observations as magnetic field reconfiguration during the current sheet thinning. Stretching of magnetic field lines results in significant bunching of all field lines crossing the equatorial PS to only a few degrees (in magnetic latitudes) at low altitudes.
2. Comparison of MMS, ARTEMIS, and ELFIN measurements of energetic electrons during current sheet thinning shows that the middle tail (MMS) and lunar orbit (ARTEMIS) PS is projected to almost the same magnetic latitudes around the edge of the outer radiation belt: there are less than 20s (less than a couple of degrees in magnetic latitude) of ELFIN observations of electron flux decreases mapping to the region from the near-Earth (THEMIS) to the lunar orbit (ARTEMIS).
3. The magnetic field reconfiguration with the field-line stretching during the current sheet thinning lasts from tens of minutes to a few hours, whereas the reconfiguration back to the quiet-time (or dipolarized) magnetotail occurs within ∼10 min. ELFIN measurements of electron fluxes right before and right after dipolarization (as determined by magnetic field dynamics at the equatorial THEMIS) show very different latitudinal (radial) distributions, that is, the thin current sheet destruction by the fast plasma flow quickly (within ∼10 min) changes the magnetic field line configuration.

These results demonstrate that magnetic field line mapping from low altitudes (or/and from the ground) to the equator is very challenging during the substorm growth phase. Mapping uncertainties may be one of the reasons for debates on the substorm onset location in the magnetotail from the ground-based observation point of view (see discussion in Donovan et al., 2008; Gabrielse et al., 2009; Lyons et al., 2013; Mende et al., 2007, 2009; Rae et al., 2009; Sergeev et al., 2012). Although a new generation of magnetic field models which include substorm dynamics (Sitnov, Stephens, et al., 2021; Stephens et al., 2019; Stephens & Sitnov, 2021; Tsyganenko et al., 2021) describes the formation of the thin current sheet and the corresponding field-line reconfiguration, uncertainties of magnetic field line mappings in such models remain unknown. ELFIN/THEMIS measurements show that the low-altitude projection of the entire PS (from the near-Earth region to the lunar orbit) shrinks to a small interface region attached to the outer radiation belt edge at low altitudes. This should significantly increase the uncertainty of any mappings, thus casting doubt on any attempt to probe the reconnection onset solely from ground-based observations. More systematic investigations of conjunctions between ground-based and equatorial signatures of current sheet thinning and dipolarization, supplemented by future experiments (see, e.g., Borovsky et al., 2020), are needed to establish ground-based signatures of the pre-onset substrom dynamics (see discussion in, e.g., Runov et al., 2021).

Acknowledgments
The authors acknowledge support by NASA awards 80NSSC21K0729 (A.V.A.), 80NSSC20K1788 (A.V.A.), 80NSSC19K0844 (X.-J.Z.), NASA contract NAS5-02099, and NSF grants AGS-1242918, AGS-2019950, and AGS-2021749 (A.V.A., X.-J.Z., and V.A.). We are grateful to NASA's CubeSat Launch Initiative for ELFIN's successful launch in the desired orbits. The authors acknowledge early support of ELFIN project by the AFOSR, under its University Nanosat Program, UNP-8 project, contract FA9453-12-D-0285, and by the California Space Grant program. We acknowledge critical contributions of numerous volunteer ELFIN team student members.

Data Availability Statement

ELFIN data is available at https://plots.elfin.ucla.edu/summary.php, THEMIS and ARTEMIS data is available at http://themis.ssl.berkeley.edu/, MMS data is available at https://lasp.colorado.edu/mms. Data access and processing was done using SPEDAS V4.1, see Angelopoulos et al. (2019).

References

An, X., Artemyev, A., Angelopoulos, V., Runov, A., Lu, S., & Pritchett, P. (2022). Configuration of magnetotail current sheet prior to magnetic reconnection onset. *Geophysical Research Letters*, *49*(6), e2022GL097870. https://doi.org/10.1029/2022GL097870

Angelopoulos, V. (2008). The THEMIS mission. *Space Science Reviews*, *141*(1–4), 5–34. https://doi.org/10.1007/s11214-008-9336-1

Angelopoulos, V. (2011). The ARTEMIS mission. *Space Science Reviews*, *165*(1–4), 3–25. https://doi.org/10.1007/s11214-010-9687-2

Angelopoulos, V., Cruce, P., Drozdov, A., Grimes, E. W., Hatzigeorgiu, N., King, D. A., et al. (2019). The space physics environment data analysis system (SPEDAS). *Space Science Reviews*, *215*(1), 9. https://doi.org/10.1007/s11214-018-0576-4

Angelopoulos, V., McFadden, J. P., Larson, D., Carlson, C. W., Mende, S. B., Frey, H., et al. (2008). Tail reconnection triggering substorm onset. *Science*, *321*(5891), 931–935. https://doi.org/10.1126/science.1160495

Angelopoulos, V., Runov, A., Zhou, X. Z., Turner, D. L., Kiehas, S. A., Li, S. S., & Shinohara, I. (2013). Electromagnetic energy conversion at reconnection fronts. *Science*, *341*(6153), 1478–1482. https://doi.org/10.1126/science.1236992

Angelopoulos, V., Sibeck, D., Carlson, C. W., McFadden, J. P., Larson, D., Lin, R. P., et al. (2008). First results from the THEMIS mission. *Space Science Reviews*, *141*(1–4), 453–476. https://doi.org/10.1007/s11214-008-9378-4

Angelopoulos, V., Tsai, E., Bingley, L., Shaffer, C., Turner, D. L., Runov, A., et al. (2020). The ELFIN mission. *Space Science Reviews*, *216*(5), 103. https://doi.org/10.1007/s11214-020-00721-7

Artemyev, A. V., Angelopoulos, V., & Runov, A. (2016). On the radial force balance in the quiet time magnetotail current sheet. *Journal of Geophysical Research*, *121*, 4017–4026. https://doi.org/10.1002/2016JA022480

Artemyev, A. V., Angelopoulos, V., Runov, A., & Petrukovich, A. A. (2016). Properties of current sheet thinning at $x \sim 10$ to 12 R_E. *Journal of Geophysical Research*, *121*, 6718–6731. https://doi.org/10.1002/2016JA022779

Artemyev, A. V., Angelopoulos, V., Runov, A., & Petrukovich, A. A. (2019). Global view of current sheet thinning: Plasma pressure gradients and large-scale currents. *Journal of Geophysical Research*, *124*, 264–278. https://doi.org/10.1029/2018JA026113

Artemyev, A. V., Petrukovich, A. A., Nakamura, R., & Zelenyi, L. M. (2013). Profiles of electron temperature and B_z along Earth's magnetotail. *Annales Geophysicae*, *31*(6), 1109–1114. https://doi.org/10.5194/angeo-31-1109-2013

Baker, D. N., Pulkkinen, T. I., Angelopoulos, V., Baumjohann, W., & McPherron, R. L. (1996). Neutral line model of substorms: Past results and present view. *Journal of Geophysical Research*, *101*(A6), 12975–13010. https://doi.org/10.1029/95JA03753

Birn, J., Dorelli, J. C., Hesse, M., & Schindler, K. (2004). Thin current sheets and loss of equilibrium: Three-dimensional theory and simulations. *Journal of Geophysical Research*, *109*, 2215. https://doi.org/10.1029/2003JA010275

Birn, J., Hesse, M., & Schindler, K. (1998). Formation of thin current sheets in space plasmas. *Journal of Geophysical Research*, *103*(A4), 6843–6852. https://doi.org/10.1029/97JA03602

Blake, J. B., Mauk, B. H., Baker, D. N., Carranza, P., Clemmons, J. H., Craft, J., et al. (2016). The Fly's Eye Energetic Particle Spectrometer (FEEPS) sensors for the Magnetospheric Multiscale (MMS) mission. *Space Science Reviews*, *199*(1–4), 309–329. https://doi.org/10.1007/s11214-015-0163-x

Borovsky, J. E., Delzanno, G. L., & Henderson, M. G. (2020). A mission concept to determine the magnetospheric causes of aurora. *Frontiers in Astronomy and Space Sciences*, *7*, 86. https://doi.org/10.3389/fspas.2020.595929

Burch, J. L., Moore, T. E., Torbert, R. B., & Giles, B. L. (2016). Magnetospheric multiscale overview and science objectives. *Space Science Reviews*, *199*(1–4), 5–21. https://doi.org/10.1007/s11214-015-0164-9

Coppi, B., Laval, G., & Pellat, R. (1966). Dynamics of the geomagnetic tail. *Physical Review Letters*, *16*(26), 1207–1210. https://doi.org/10.1103/PhysRevLett.16.1207

Delcourt, D. C., Belmont, G., Sauvaud, J.-A., Moore, T. E., & Martin, R. F. (1996). Centrifugally driven phase bunching and related current sheet structure in the near-Earth magnetotail. *Journal of Geophysical Research*, *101*(A9), 19839–19847. https://doi.org/10.1029/96JA01772

Delcourt, D. C., Martin, R. F., Jr., & Alem, F. (1994). A simple model of magnetic moment scattering in a field reversal. *Geophysical Research Letters*, *21*(14), 1543–1546. https://doi.org/10.1029/94GL01291

Donovan, E., Liu, W., Liang, J., Spanswick, E., Voronkov, I., Connors, M., et al. (2008). Simultaneous THEMIS in situ and auroral observations of a small substorm. *Geophysical Research Letters*, *35*(17), L17S18. https://doi.org/10.1029/2008GL033794

Dubyagin, S., Apatenkov, S., Gordeev, E., Ganushkina, N., & Zheng, Y. (2021). Conditions of loss cone filling by scattering on the curved field lines for 30 keV protons during geomagnetic storm as inferred from numerical trajectory tracing. *Journal of Geophysical Research*, *126*, e28490. https://doi.org/10.1029/2020JA028490

Dubyagin, S., Ganushkina, N. Y., & Sergeev, V. (2018). Formation of 30 KeV proton isotropic boundaries during geomagnetic storms. *Journal of Geophysical Research*, *123*, 3436–3459. https://doi.org/10.1002/2017JA024587

Dubyagin, S., Sergeev, V. A., & Kubyshkina, M. V. (2002). On the remote sensing of plasma sheet from low-altitude spacecraft. *Journal of Atmospheric and Solar-Terrestrial Physics*, *64*(5–6), 567–572. https://doi.org/10.1016/S1364-6826(02)00014-7

Gabrielse, C., Angelopoulos, V., Harris, C., Artemyev, A., Kepko, L., & Runov, A. (2017). Extensive electron transport and energization via multiple, localized dipolarizing flux bundles. *Journal of Geophysical Research*, *122*, 5059–5076. https://doi.org/10.1002/2017JA023981

Gabrielse, C., Angelopoulos, V., Runov, A., Frey, H. U., McFadden, J., Larson, D. E., et al. (2009). Timing and localization of near-Earth tail and ionospheric signatures during a substorm onset. *Journal of Geophysical Research*, *114*, A00C13. https://doi.org/10.1029/2008JA013583

Gabrielse, C., Angelopoulos, V., Runov, A., & Turner, D. L. (2014). Statistical characteristics of particle injections throughout the equatorial magnetotail. *Journal of Geophysical Research*, *119*, 2512–2535. https://doi.org/10.1002/2013JA019638

Gabrielse, C., Spanswick, E., Artemyev, A., Nishimura, Y., Runov, A., Lyons, L., et al. (2019). Utilizing the Heliophysics/Geospace system observatory to understand particle injections: Their scale sizes and propagation directions. *Journal of Geophysical Research*, *124*, 5584–5609. https://doi.org/10.1029/2018JA025588

Galeev, A. A., & Zelenyĭ, L. M. (1977). Model of magnetic-field reconnection in a plane layer of collisionless plasma. *Soviet Journal of Experimental and Theoretical Physics Letters*, *25*, 380.

Gordeev, E., Sergeev, V., Merkin, V., & Kuznetsova, M. (2017). On the origin of plasma sheet reconfiguration during the substorm growth phase. *Geophysical Research Letters*, *44*(17), 8696–8702. https://doi.org/10.1002/2017GL074539

Hsieh, M.-S., & Otto, A. (2015). Thin current sheet formation in response to the loading and the depletion of magnetic flux during the substorm growth phase. *Journal of Geophysical Research*, *120*, 4264–4278. https://doi.org/10.1002/2014JA020925

Imhof, W. L., Reagan, J. B., & Gaines, E. E. (1977). Fine-scale spatial structure in the pitch angle distributions of energetic particles near the midnight trapping boundary. *Journal of Geophysical Research*, *82*(32), 5215–5221. https://doi.org/10.1029/JA082i032p05215

Khazanov, G. V., Sibeck, D. G., & Zesta, E. (2017). Major pathways to electron distribution function formation in regions of diffuse aurora. *Journal of Geophysical Research*, *122*, 4251–4265. https://doi.org/10.1002/2017JA023956

Kozelova, T. V., & Kozelov, B. V. (2013). Substorm-associated explosive magnetic field stretching near the earthward edge of the plasma sheet. *Journal of Geophysical Research*, *118*, 3323–3335. https://doi.org/10.1002/jgra.50344

Lessard, M. R., Lotko, W., LaBelle, J., Peria, W., Carlson, C. W., Creutzberg, F., & Wallis, D. D. (2007). Ground and satellite observations of the evolution of growth phase auroral arcs. *Journal of Geophysical Research*, *112*, A09304. https://doi.org/10.1029/2006JA011794

Liu, Y.-H., Birn, J., Daughton, W., Hesse, M., & Schindler, K. (2014). Onset of reconnection in the near magnetotail: PIC simulations. *Journal of Geophysical Research*, *119*, 9773–9789. https://doi.org/10.1002/2014JA020492

Lu, S., Artemyev, A. V., Angelopoulos, V., Lin, Y., Zhang, X. J., Liu, J., et al. (2019). The hall electric field in Earth's magnetotail thin current sheet. *Journal of Geophysical Research*, *124*, 1052–1062. https://doi.org/10.1029/2018JA026202

Lu, S., Artemyev, A. V., Angelopoulos, V., Pritchett, P. L., & Runov, A. (2019). Effects of cross-sheet density and temperature inhomogeneities on magnetotail Reconnection. *Geophysical Research Letters*, *46*(1), 28–36. https://doi.org/10.1029/2018GL081420

Lu, S., Lin, Y., Angelopoulos, V., Artemyev, A. V., Pritchett, P. L., Lu, Q., & Wang, X. Y. (2016). Hall effect control of magnetotail dawn-dusk asymmetry: A three-dimensional global hybrid simulation. *Journal of Geophysical Research*, *121*, 11. https://doi.org/10.1002/2016JA023325

Lu, S., Pritchett, P. L., Angelopoulos, V., & Artemyev, A. V. (2018). Formation of dawn-dusk asymmetry in Earth's magnetotail thin current sheet: A three-dimensional particle-in-cell simulation. *Journal of Geophysical Research*, *123*, 2801–2814. https://doi.org/10.1002/2017JA025095

Lu, S., Wang, R., Lu, Q., Angelopoulos, V., Nakamura, R., Artemyev, A. V., et al. (2020). Magnetotail reconnection onset caused by electron kinetics with a strong external driver. *Nature Communications*, *11*(1), 5049. https://doi.org/10.1038/s41467-020-18787-w

Lyons, L. R., Nishimura, Y., Donovan, E., & Angelopoulos, V. (2013). Distinction between auroral substorm onset and traditional ground magnetic onset signatures. *Journal of Geophysical Research*, *118*, 4080–4092. https://doi.org/10.1002/jgra.50384

Ma, Q., Li, W., Thorne, R. M., Bortnik, J., Reeves, G. D., Kletzing, C. A., et al. (2016). Characteristic energy range of electron scattering due to plasmaspheric hiss. *Journal of Geophysical Research*, *121*, 11. https://doi.org/10.1002/2016JA023311

Mende, S. B., Angelopoulos, V., Frey, H. U., Donovan, E., Jackel, B., Glassmeier, K. H., et al. (2009). Timing and location of substorm onsets from THEMIS satellite and ground based observations. *Annales Geophysicae*, *27*(7), 2813–2830. https://doi.org/10.5194/angeo-27-2813-2009

Mende, S. B., Angelopoulos, V., Frey, H. U., Harris, S., Donovan, E., Jackel, B., et al. (2007). Determination of substorm onset timing and location using the THEMIS ground based observatories. *Geophysical Research Letters*, *34*(17), 17108. https://doi.org/10.1029/2007GL030850

Mitchell, D. G., Williams, D. J., Huang, C. Y., Frank, L. A., & Russell, C. T. (1990). Current carriers in the near-Earth cross-tail current sheet during substorm growth phase. *Geophysical Research Letters*, *17*(5), 583–586. https://doi.org/10.1029/GL017i005p00583

Mourenas, D., Artemyev, A. V., Zhang, X. J., Angelopoulos, V., Tsai, E., & Wilkins, C. (2021). Electron lifetimes and diffusion rates inferred from ELFIN measurements at low altitude: First results. *Journal of Geophysical Research*, *126*, e29757. https://doi.org/10.1029/2021JA029757

Mourenas, D., Ma, Q., Artemyev, A. V., & Li, W. (2017). Scaling laws for the inner structure of the radiation belts. *Geophysical Research Letters*, *44*(7), 3009–3018. https://doi.org/10.1002/2017GL072987

Nakamura, R., Baumjohann, W., Panov, E., Volwerk, M., Birn, J., Artemyev, A., et al. (2013). Flow bouncing and electron injection observed by Cluster. *Journal of Geophysical Research*, *118*, 2055–2072. https://doi.org/10.1002/jgra.50134

Nakamura, R., Retinò, A., Baumjohann, W., Volwerk, M., Erkaev, N., Klecker, B., et al. (2009). Evolution of dipolarization in the near-Earth current sheet induced by Earthward rapid flux transport. *Annales Geophysicae*, *27*(4), 1743–1754. https://doi.org/10.5194/angeo-27-1743-2009

Newell, P. T., Sergeev, V. A., Bikkuzina, G. R., & Wing, S. (1998). Characterizing the state of the magnetosphere: Testing the ion precipitation maxima latitude (b2i) and the ion isotropy boundary. *Journal of Geophysical Research*, *103*(A3), 4739–4746. https://doi.org/10.1029/97JA03622

Ni, B., Thorne, R. M., Zhang, X., Bortnik, J., Pu, Z., Xie, L., et al. (2016). Origins of the Earth's diffuse auroral precipitation. *Space Science Reviews*, *200*(1–4), 205–259. https://doi.org/10.1007/s11214-016-0234-7

Nishimura, Y., Lessard, M. R., Katoh, Y., Miyoshi, Y., Grono, E., Partamies, N., et al. (2020). Diffuse and pulsating aurora. *Space Science Reviews*, *216*(1), 4. https://doi.org/10.1007/s11214-019-0629-3

Pellat, R., Coroniti, F. V., & Pritchett, P. L. (1991). Does ion tearing exist? *Geophysical Research Letters*, *18*(2), 143–146. https://doi.org/10.1029/91GL00123

Petrukovich, A. A., Artemyev, A. V., Nakamura, R., Panov, E. V., & Baumjohann, W. (2013). Cluster observations of dB_z/dx during growth phase magnetotail stretching intervals. *Journal of Geophysical Research*, *118*, 5720–5730. https://doi.org/10.1002/jgra.50550

Petrukovich, A. A., Baumjohann, W., Nakamura, R., Runov, A., Balogh, A., & Rème, H. (2007). Thinning and stretching of the plasma sheet. *Journal of Geophysical Research*, *112*, 10213. https://doi.org/10.1029/2007JA012349

Pritchett, P. L. (2005). Externally driven magnetic reconnection in the presence of a normal magnetic field. *Journal of Geophysical Research*, *110*, 5209. https://doi.org/10.1029/2004JA010948

Pritchett, P. L., & Coroniti, F. V. (2011). Plasma sheet disruption by interchange-generated flow intrusions. *Geophysical Research Letters*, *381*(10), 10102. https://doi.org/10.1029/2011GL047527

Pritchett, P. L., Coroniti, F. V., & Pellat, R. (1997). Convection-driven reconnection and the stability of the near-Earth plasma sheet. *Geophysical Research Letters*, *24*(8), 873–876. https://doi.org/10.1029/97GL00672

Pritchett, P. L., Coroniti, F. V., Pellat, R., & Karimabadi, H. (1991). Collisionless reconnection in two-dimensional magnetotail equilibria. *Journal of Geophysical Research*, *96*(A7), 11. https://doi.org/10.1029/91JA01094

Rae, I. J., Mann, I. R., Angelopoulos, V., Murphy, K. R., Milling, D. K., Kale, A., et al. (2009). Near-Earth initiation of a terrestrial substorm. *Journal of Geophysical Research*, *114*, A07220. https://doi.org/10.1029/2008JA013771

Runov, A., Angelopoulos, V., Artemyev, A. V., Weygand, J. M., Lu, S., Lin, Y., & Zhang, X. J. (2021). Global and local processes of thin current sheet formation during substorm growth phase. *Journal of Atmospheric and Solar-Terrestrial Physics*, *220*, 105671. https://doi.org/10.1016/j.jastp.2021.105671

Runov, A., Angelopoulos, V., Sitnov, M. I., Sergeev, V. A., Bonnell, J., McFadden, J. P., et al. (2009). THEMIS observations of an Earthward-propagating dipolarization front. *Geophysical Research Letters*, *36*(14), L14106. https://doi.org/10.1029/2009GL038980

Runov, A., Angelopoulos, V., Zhou, X.-Z., Zhang, X.-J., Li, S., Plaschke, F., & Bonnell, J. (2011). A THEMIS multicase study of dipolarization fronts in the magnetotail plasma sheet. *Journal of Geophysical Research*, *116*, 5216. https://doi.org/10.1029/2010JA016316

Russell, C. T., Anderson, B. J., Baumjohann, W., Bromund, K. R., Dearborn, D., Fischer, D., et al. (2016). The magnetospheric multiscale magnetometers. *Space Science Reviews*, *199*(1–4), 189–256. https://doi.org/10.1007/s11214-014-0057-3

Samson, J. C., Lyons, L. R., Newell, P. T., Creutzberg, F., & Xu, B. (1992). Proton aurora and substorm intensifications. *Geophysical Research Letters*, *19*(21), 2167–2170. https://doi.org/10.1029/92GL02184

Sanny, J., McPherron, R. L., Russell, C. T., Baker, D. N., Pulkkinen, T. I., & Nishida, A. (1994). Growth-phase thinning of the near-Earth current sheet during the CDAW 6 substorm. *Journal of Geophysical Research*, *99*(A4), 5805–5816. https://doi.org/10.1029/93JA03235

Sarafopoulos, D. V., Sidiropoulos, N. F., Sarris, E. T., Lutsenko, V., & Kudela, K. (2001). The dawn-dusk plasma sheet asymmetry of energetic particles: An interball perspective. *Journal of Geophysical Research*, *106*(A7), 13053–13066. https://doi.org/10.1029/2000JA900157

Schindler, K. (1974). A theory of the substorm mechanism. *Journal of Geophysical Research*, *79*(19), 2803–2810. https://doi.org/10.1029/JA079i019p02803

Schindler, K., & Birn, J. (1982). Self-consistent theory of time-dependent convection in the Earth's magnetotail. *Journal of Geophysical Research*, *87*(A4), 2263–2275. https://doi.org/10.1029/JA087iA04p02263

Schindler, K., & Birn, J. (1993). On the cause of thin current sheets in the near-Earth magnetotail and their possible significance for magnetospheric substorms. *Journal of Geophysical Research*, *98*(A9), 15. https://doi.org/10.1029/93JA01047

Sergeev, V. A., Angelopoulos, V., Kubyshkina, M., Donovan, E., Zhou, X.-Z., Runov, A., et al. (2011). Substorm growth and expansion onset as observed with ideal ground-spacecraft THEMIS coverage. *Journal of Geophysical Research*, *116*, A00I26. https://doi.org/10.1029/2010JA015689

Sergeev, V. A., Chernyaev, I. A., Angelopoulos, V., & Ganushkina, N. Y. (2015). Magnetospheric conditions near the equatorial footpoints of proton isotropy boundaries. *Annales Geophysicae*, *33*(12), 1485–1493. https://doi.org/10.5194/angeo-33-1485-2015

Sergeev, V. A., Gordeev, E. I., Merkin, V. G., & Sitnov, M. I. (2018). Does a local B-Minimum appear in the tail current sheet during a substorm growth phase? *Geophysical Research Letters*, *45*(6), 2566–2573. https://doi.org/10.1002/2018GL077183

Sergeev, V. A., Malkov, M., & Mursula, K. (1993). Testing the isotropic boundary algorithm method to evaluate the magnetic field configuration in the tail. *Journal of Geophysical Research*, *98*(A5), 7609–7620. https://doi.org/10.1029/92JA02587

Sergeev, V. A., Mitchell, D. G., Russell, C. T., & Williams, D. J. (1993). Structure of the tail plasma/current sheet at ~11R_E and its changes in the course of a substorm. *Journal of Geophysical Research*, *98*(A10), 17345–17366. https://doi.org/10.1029/93JA01151

Sergeev, V. A., Nishimura, Y., Kubyshkina, M., Angelopoulos, V., Nakamura, R., & Singer, H. (2012). Magnetospheric location of the equatorward prebreakup arc. *Journal of Geophysical Research*, *117*, A01212. https://doi.org/10.1029/2011JA017154

Sergeev, V. A., Sazhina, E. M., Tsyganenko, N. A., Lundblad, J. A., & Soraas, F. (1983). Pitch-angle scattering of energetic protons in the magnetotail current sheet as the dominant source of their isotropic precipitation into the nightside ionosphere. *Planatary Space Science*, *31*(10), 1147–1155. https://doi.org/10.1016/0032-0633(83)90103-4

Sergeev, V. A., & Tsyganenko, N. A. (1982). Energetic particle losses and trapping boundaries as deduced from calculations with a realistic magnetic field model. *Planatary Space Science*, *30*(10), 999–1006. https://doi.org/10.1016/0032-0633(82)90149-0

Sitnov, M. I., Birn, J., Ferdousi, B., Gordeev, E., Khotyaintsev, Y., Merkin, V., et al. (2019). Explosive magnetotail activity. *Space Science Reviews*, *215*(4), 31. https://doi.org/10.1007/s11214-019-0599-5

Sitnov, M. I., Buzulukova, N., Swisdak, M., Merkin, V. G., & Moore, T. E. (2013). Spontaneous formation of dipolarization fronts and reconnection onset in the magnetotail. *Geophysical Research Letters*, *40*(1), 22–27. https://doi.org/10.1029/2012GL054701

Sitnov, M. I., Merkin, V. G., Pritchett, P. L., & Swisdak, M. (2017). Distinctive features of internally driven magnetotail reconnection. *Geophysical Research Letters*, *44*(7), 3028–3037. https://doi.org/10.1002/2017GL072784

Sitnov, M. I., Motoba, T., & Swisdak, M. (2021). Multiscale nature of the magnetotail reconnection onset. *Geophysical Research Letters*, *48*(10), e93065. https://doi.org/10.1029/2021GL093065

Sitnov, M. I., Sharma, A. S., Guzdar, P. N., & Yoon, P. H. (2002). Reconnection onset in the tail of Earth's magnetosphere. *Journal of Geophysical Research*, *107*(A9), 1256. https://doi.org/10.1029/2001JA009148

Sitnov, M. I., Stephens, G., Motoba, T., & Swisdak, M. (2021). Data mining reconstruction of magnetotail reconnection and implications for its first-principle modeling. *Frontiers in Physics*, *9*, 90. https://doi.org/10.3389/fphy.2021.644884

Snekvik, K., Tanskanen, E., Østgaard, N., Juusola, L., Laundal, K., Gordeev, E. I., & Borg, A. L. (2012). Changes in the magnetotail configuration before near-Earth reconnection. *Journal of Geophysical Research*, *117*, 2219. https://doi.org/10.1029/2011JA017040

Stephens, G. K., & Sitnov, M. I. (2021). Concurrent empirical magnetic reconstruction of storm and substorm spatial scales using data mining and virtual spacecraft. *Frontiers in Physics*, *9*, 210. https://doi.org/10.3389/fphy.2021.653111

Stephens, G. K., Sitnov, M. I., Korth, H., Tsyganenko, N. A., Ohtani, S., Gkioulidou, M., & Ukhorskiy, A. Y. (2019). Global empirical picture of magnetospheric substorms inferred from multimission magnetometer data. *Journal of Geophysical Research*, *124*, 1085–1110. https://doi.org/10.1029/2018JA025843

Sun, W. J., Fu, S. Y., Wei, Y., Yao, Z. H., Rong, Z. J., Zhou, X. Z., et al. (2017). Plasma sheet pressure variations in the near-Earth magnetotail during substorm growth phase: Themis observations. *Journal of Geophysical Research*, *122*, 12212–12228. https://doi.org/10.1002/2017JA024603

Tsyganenko, N. A. (1989). A magnetospheric magnetic field model with a warped tail current sheet. *Planatary Space Science*, *37*(1), 5–20. https://doi.org/10.1016/0032-0633(89)90066-4

Tsyganenko, N. A., Andreeva, V. A., Sitnov, M. I., Stephens, G. K., Gjerloev, J. W., Chu, X., & Troshichev, O. A. (2021). Reconstructing substorms via historical data mining: Is it really feasible? *Journal of Geophysical Research: Space Physics*, *126*, e2021JA029604. https://doi.org/10.1029/2021JA029604

Voronkov, I., Friedrich, E., & Samson, J. C. (1999). Dynamics of the substorm growth phase as observed using CANOPUS and SuperDARN instruments. *Journal of Geophysical Research*, *104*(A12), 28491–28504. https://doi.org/10.1029/1999JA900362

Wanliss, J. A., Samson, J. C., & Friedrich, E. (2000). On the use of photometer data to map dynamics of the magnetotail current sheet during substorm growth phase. *Journal of Geophysical Research*, *105*(A12), 27673–27684. https://doi.org/10.1029/2000JA000178

Yahnin, A. G., Sergeev, V. A., Gvozdevsky, B. B., & Vennerstrøm, S. (1997). Magnetospheric source region of discrete auroras inferred from their relationship with isotropy boundaries of energetic particles. *Annales Geophysicae*, *15*(8), 943–958. https://doi.org/10.1007/s00585-997-0943-z

Yue, C., Wang, C.-P., Nishimura, Y., Murphy, K. R., Xing, X., Lyons, L., et al. (2015). Empirical modeling of 3-D force-balanced plasma and magnetic field structures during substorm growth phase. *Journal of Geophysical Research*, *120*, 6496–6513. https://doi.org/10.1002/2015JA021226

Yushkov, E., Petrukovich, A., Artemyev, A., & Nakamura, R. (2021). Thermodynamics of the magnetotail current sheet thinning. *Journal of Geophysical Research: Space Physics*, *126*, e2020JA028969. https://doi.org/10.1029/2020JA028969

Zelenyi, L. M., Artemyev, A. V., Malova, H. V., & Popov, V. Y. (2008). Marginal stability of thin current sheets in the Earth's magnetotail. *Journal of Atmospheric and Solar-Terrestrial Physics*, *70*(2–4), 325–333. https://doi.org/10.1016/j.jastp.2007.08.019